Solar Physics (2026) 301:25
https://doi.org/10.1007/s11207-026-02613-5

RESEARCH

Automatic Detection of CMEs Using Synthetically-Trained Mask R-CNN

Francisco A. Iglesias[1,2] · Diego G. Lloveras[1,2,3,4] · Florencia L. Cisterna[1] · Hebe Cremades[1,2] · Mariano Sanchez Toledo[1] · Fernando M. López[1,2] · Yasmin Machuca[1,2] · Franco Manini[1,2] · Andrés Asensio Ramos[5]

Received: 5 November 2025 / Accepted: 11 January 2026 / Published online: 10 February 2026
© US Government 2026

Abstract

Coronal mass ejections (CMEs) are a major driver of space weather. To assess CME geoeffectiveness, among other scientific goals, it is necessary to reliably identify and characterize their morphology and kinematics in coronagraph images. Current methods of CME identification are either subjected to human biases or perform a poor identification due to deficiencies in the automatic detection. In this approach, we have trained the deep convolutional neural model Mask R-CNN to automatically segment the outer envelope of one or multiple CMEs present in a single difference coronagraph image. The empirical training dataset is composed of 1.13×10^5 synthetic coronagraph images with known pixel-level CME segmentation masks. It is obtained by combining quiet (no CME) coronagraph observations, with synthetic white-light CMEs produced using the Graduated Cylindrical Shell geometric model and ray-tracing technique. To filter the different instances found by Mask R-CNN, we use the temporal consistency of mask properties such as the intersection over union (IoU). We found that our model-based trained Mask R-CNN infers segmentation masks that are smooth and topologically connected (without holes or isolated patches). While the inferred masks are not representative of the detailed outer envelope of complex CMEs, the neural model can better differentiate a CME from other radially moving background/foreground features, segment multiple simultaneous CMEs that are close to each other, and work with images from different instruments. This is accomplished without relying on kinematic information, i.e. only the included in the single input difference image. We obtain a median $IoU = 0.98$ for 1.6×10^4 synthetic validation images, and $IoU = 0.77$ when compared with two independent manual segmentations of 115 observations acquired by the COR2-A, COR2-B, and LASCO C2 coronagraphs. The methodology presented in this work can be used with other CME models to produce more realistic synthetic brightness images while preserving desired morphological features, and obtain more robust and/or tailored segmentations.

Keywords Sun: coronal mass ejections (CMEs) · Methods: machine learning · Methods: data analysis

Francisco A. Iglesias and Diego G. Lloveras contributed equally to this work.

Extended author information available on the last page of the article

1. Introduction

Coronal Mass Ejections (CMEs) involve the fast release of large amounts of mass and magnetic field from the solar corona into the interplanetary medium (Webb and Howard 2012). They produce significant perturbations in the solar wind and strongly influence space weather, with important detrimental impacts on various critical technologies (Zhang et al. 2018). Due to the lack of routine magnetic-field measurements of the solar corona (Judge et al. 2001), among other reasons, no clear consensus has been reached regarding which are the predominant CME trigger and driving mechanisms (Green et al. 2018). This and other limitations result in our current inability to forecast when and where on the solar surface the next CME is going to take place. Subsequently, it becomes critical to estimate the morphology and kinematics of CMEs as early as possible after their onset; in order to elaborate better predictions of their arrival time to Earth and geo-effectiveness.

CMEs manifest in white-light coronagraphs as bright radially-moving structures ejected from the Sun on timescales of minutes to several hours. Some emblematic space-based solar coronagraphs are the Large Angle and Spectrometric Coronagraph (LASCO; Brueckner et al. 1995) onboard the Solar and Heliospheric Observatory (SoHO), which is located near the Lagrangian point L1; and the coronagraphs COR1 and COR2 part of the Sun-Earth Connection Coronal and Heliospheric Investigation (SECCHI; Howard et al. 2008) package onboard the Solar-TErrestrial RElations Observatory (STEREO) twin spacecraft, that enables observing CMEs from different perspectives in the ecliptic plane. Since their initial detection in the 1970s, there have been many efforts devoted to identify and characterize CMEs in white-light coronagraphic images, using various manual or automated techniques. We classify these techniques into three categories and summarize them below.

Manual: Performed by an educated operator, such as in the LASCO CME Catalog[1] of the Coordinated Data Analysis Workshops (CDAW) Data Center (Yashiro et al. 2004; Gopalswamy et al. 2009). This approach can deal with complex scenarios that typically complicate image processing algorithms, such as events with fast-moving background material and/or multiple quasi-simultaneous events. On the other hand, manual inspection is subjective and thus not free of errors (e.g., Yashiro, Michalek, and Gopalswamy 2008). It is also time-consuming and impractical to apply to the large data volumes generated by present and proposed coronagraphs, such as the MOST (Gopalswamy et al. 2024) and Vigil missions (Palomba and Luntama 2022).

Image processing: This approach uses traditional image processing techniques, mostly based on pixel brightness spatio-temporal variations and fine-tuned filtering, performed in the height-time map associated to the event. This is done, for example, in the pioneering Computer-Aided CME Tracking method (CACTus; Robbrecht, Patsourakos, and Vourlidas 2009),[2] the Solar Eruptive Event Detection System (SEEDS; Olmedo et al. 2008),[3] the CORonal IMage Process (CORIMP; Byrne et al. 2012),[4] the Automatic Recognition of Transient Events and Marseille Inventory from Synoptic maps (ARTEMIS; Boursier et al. 2009),[5] and the CORonal SEgmentation Technique (CORSET; Goussies et al. 2010) used at the multi-viewpoint STEREO catalog[6] by Vourlidas et al. (2017). These image processing

[1] cdaw.gsfc.nasa.gov/CME_list/index.html.

[2] sidc.oma.be/cactus/.

[3] spaceweather.gmu.edu/seeds/.

[4] alshamess.ifa.hawaii.edu/CORIMP/.

[5] cesam.lam.fr/lascomission/ARTEMIS/.

[6] solar.jhuapl.edu/Data-Products/COR-CME-Catalog.php.

techniques have the advantage of being automatic or semi-automatic, with faster and easier implementation than manual inspection, and have resulted in useful CME catalogs (see the citations above). However, these algorithms generally fail in common cases, where the spatial and temporal brightness variation of CME and background/foreground moving material are difficult to distinguish from each other, see e.g., Yashiro, Michalek, and Gopalswamy (2008) and Vourlidas et al. (2017).

Machine learning: Machine Learning (ML) has experienced enormous improvements during the last decade. Models involving Deep Convolutional Neural Networks (DCNNs) currently excel at solving machine-vision related tasks. This has led to various applications of ML to different topics in solar physics and space weather, as reviewed by Camporeale (2019) and Asensio Ramos et al. (2023). The automatic detection of CMEs in coronagraph images using ML was pioneered by Wang et al. (2019), further explored by Alshehhi and Marpu (2021) and very recently by Lin et al. (2024), Shan et al. (2024), and Bauer et al. (2025). We summarize these and the present works in the diagram shown in Figure 1.

In the efforts grouped under approach A, a DCNN-based classifier is first trained to label images as CME or non-CME, typically using a backbone plus a fully connected head. Wang et al. (2019) and Lin et al. (2024) employ as backbone LeNet trained on manually classified LASCO CDAW images, whereas Alshehhi and Marpu (2021) use the VGG16 model (Simonyan and Zisserman 2014) already trained for classification with the Imagenet database (Deng et al. 2009), which does not contain CME images. The deep feature maps from the classifier are then repurposed to derive a coarse mask precursor in an unsupervised manner: for each image of the event a feature map is extracted, and Principal Components Analysis (PCA) is applied to exploit spatio–temporal correlations. Wang et al. (2019) and Lin et al. (2024) implement the PCA-based image co-location method of Wei et al. (2019), while Alshehhi and Marpu (2021) combine PCA with K-means clustering. This precursor is converted into a binary mask via post-processing. Wang et al. (2019) use a graph-cut formulation that also accounts for temporal expansion; Alshehhi and Marpu (2021) apply morphological erosion and dilation to smooth and improve connectivity; and Lin et al. (2024) threshold using Otsu's method (Otsu 1979) followed by the same morphological operators. Finally, a tracking stage enforces temporal consistency and removes spurious regions by leveraging expected CME behavior (e.g., outward motion, small central position angle changes). Wang et al. (2019) and Alshehhi and Marpu (2021) discard all pixels at position angles whose maximum height is less than half the image field of view, and reject any CME candidate that does not move outward in at least two consecutive frames or does not extend beyond the LASCO C2 field of view (following Olmedo et al. 2008). On the other hand, Lin et al. (2024) adopts a more general similarity metric, based on a weighted sum of differences in geometric centers, areas, and shape descriptors (the latter following Chaumette 2004).

Two alternatives to approach A are using fully unsupervised learning, e.g., with an autoencoder architecture (Xia and Kulis 2017), not explored so far; or producing a suitable training dataset for supervised segmentation, i.e. including a known true mask for each image. Supervised segmentation has the advantage that the error between inferred ($\bar{M}$) and true (M) masks can be quantified using common metrics, such as Intersection over Union (IoU) or the Relative Symmetric Difference (RSD), see e.g., Reinke et al. (2021):

$$IoU = \frac{\bar{M} \cap M}{\bar{M} \cup M}, \; RSD = \frac{\bar{M} \cup M - \bar{M} \cap M}{M}. \tag{1}$$

Training data can be generated via manual pixel-level labeling done by a human operator, or synthetically, using a coronal and/or CME model. The former was explored recently by

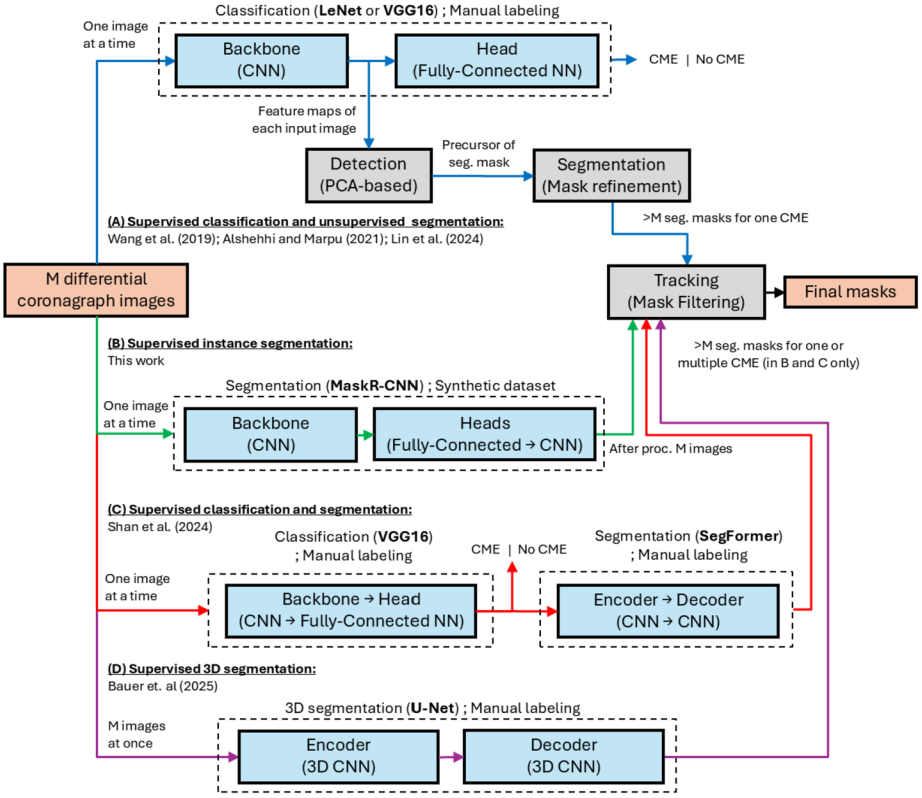


Figure 1 ML-based segmentation of CMEs. We summarize current approaches found in the literature, including supervised classification followed by unsupervised segmentation (A, blue arrows), supervised classification followed by supervised segmentation using manually labeled data (C, red arrows), and supervised 3D segmentation using manually labeled data (D, violet arrows). The supervised instance segmentation approach used in this work (B, green arrows) employs synthetic data instead of manual labeling. We sketch a simplified version of the data flow between blocks representing input/output (orange), different NNs (blue), and other processing algorithms (grey). The designation of each approach and the name of the neural model used are annotated in bold. See the text for extra details.

Shan et al. (2024), approach C in Figure 1, who manually labeled 375 LASCO C2 images to train the SegFromer model (Xie et al. 2021); and by Bauer et al. (2025), approach D in Figure 1, who produced ≈ 8400 labels for images of the Heliospheric Imagers (HI, Eyles et al. 2009) onboard STEREO and trained the 3D U-Net model (Ronneberger, Fischer, and Brox 2015). Shan et al. (2024) introduce an improved multi-CME tracking algorithm and report $IoU = 0.83$, which is a significant improvement with respect to the 0.49 of their previous work in Wang et al. (2019). Shan et al. (2024) have also released a 2D segmentation catalog, and used this technique to produce also a 3D CME catalog, see the reference for further details. On the other hand, Bauer et al. (2025) uses a beneficial 3D DCNN that allows processing multiple images of a single event at once and reports $IoU = 0.39$. We note that the latter uses data from HI, which observes CMEs much farther from the Sun (up to 330 $R_{\odot}$), and thus the images are typically noisier, and the fainter CMEs are considerably more difficult to differentiate from moving background/foreground material.

The works presented in Figure 1, and briefly described above, are important contributions to the advancement of automatic CME segmentation and characterization. Their results show that ML-based approaches are generally better than image processing algorithms at detecting weaker CMEs in earlier stages, smaller changes in the identified CME region, CMEs in more complex scenarios such as those containing fast-moving background/foreground material, and CMEs with smaller angular widths. Alshehhi and Marpu (2021) also shows that their method is closer to the results of the manual CDAW catalog than to those of the CACTus and CORIMP algorithms for 2000 random CMEs.

Besides these promising results, there are still limitations. In approach A, the final segmentation mask properties are strongly influenced by the unsupervised algorithms that derive them from the neural feature maps. The same occurs with the algorithms used for mask filtering in the tracking step of approaches C and D. These algorithms are based on spatio-temporal correlation plus filtering and thresholding, making it difficult to generalize to all CME cases and stages of the solar cycle, resulting in common errors where nearby moving background/foreground material is segmented as part of the CME bulk. On the other hand, the subjective manual labeling of Shan et al. (2024) and Bauer et al. (2025) also presents disadvantages, some already pointed out by the authors. The labeling process is very time-consuming, and different operators can produce different masks for slow and/or faint CMEs that do not present a strong contrast with respect to the background, among other subjective effects. In addition, there is no precise definition of the CME boundary, which harms the usage of quantitative error metrics to compare the performance of different methods in a systematic manner.

In this work, denoted approach B in Figure 1, we explore the usage of synthetic data for supervised training. This has been successfully done in other Solar Physics applications, such as spectropolarimetric Stokes inversions (Milić and Gafeira 2020; Gafeira et al. 2021) and photospheric velocity estimations (Asensio Ramos, Requerey, and Vitas 2017), among others. Our approach implies generating a dataset composed of synthetic CME coronagraph images with known pixel-level segmentation masks, using it to train a commercial-off-the-shelf Deep Neural Network (DNN) to perform CME segmentation, and using the trained model to infer CME masks from real coronagraph images. Even when this approach presents limitations related to the quality of the empirical synthetic data, see Section 2, it also helps tackling some of the drawbacks discussed above. Particularly those related to incorporating high-level morphological properties of the CME mask to help better differentiate it from other moving material, and thus relies less on the mask filtering step. We demonstrate the potential of this approach using synthetic data based on a simple morphological CME model, namely the Graduated Cylindrical Shell (GCS, see Section 2), in combination with ray-tracing. However, the same approach can be used with any other model that allows generating, potentially more realistic, synthetic CME brightness images and their corresponding masks.

The rest of the paper is organized as follows. Section 2 details the generation of the synthetic training data set (Section 2.1), the architecture and training of the DNN used for CME segmentation (Section 2.2). The results are presented and discussed in Section 3, including the performance on synthetic (Section 3.1) and manually segmented CME observations (Section 3.2). The conclusions and outlook are given in Section 4.

2. Data and Methods

The synthetic images, generated for training purposes, are formed by adding a synthetic CME differential brightness image to a differential background image taken from archive

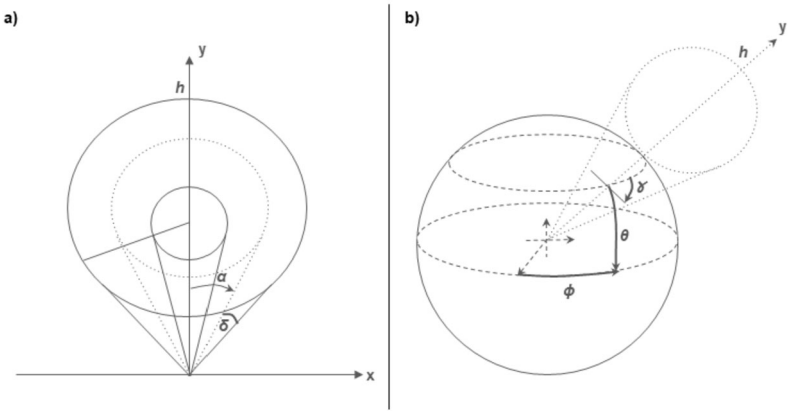


Figure 2 The GCS geometric model, including its face-on view (*panel a*) and a 3D perspective showing the source region on the solar surface (*panel b*). The 6 model parameters are the source region Stonyhurst longitude (ϕ) and heliographic latitude (θ), tilt angle with respect to the local parallel (γ), height of the apex (h), aspect ratio (κ), and half angular separation of the legs (α). Adapted from Thernisien, Vourlidas, and Howard (2009).

coronagraph observations. The synthetic CME images are based on the empirical Graduated Cylindrical Shell model (GCS, Thernisien, Howard, and Vourlidas 2006), which defines a 3D geometric shape to describe the flux rope structure of CMEs. The GCS has a "croissant-like" shape, with a circular cross section and two conical legs anchored to the center of the Sun (see Figure 2). The 3D shape and its position are completely defined by the six following parameters:

- ϕ, θ: Stonyhurst longitude and Heliographic latitude of the intersection point between the GCS main axis and the solar surface, respectively.
- γ: Tilt angle with respect to the local parallel.
- h: Height of the apex.
- $\kappa = \sin\delta$: Aspect ratio, where δ is the half angular width of the legs.
- α: Half the angular separation of the legs.

The GCS is unable to model in detail the outer shell shape of complex CMEs. However, with only six degrees of freedom, the model defines a topologically connected shape that retains important basic properties attributed to CMEs, such as a self-similar bulk expansion. The GCS is widely used to reconstruct the 3D structure of the CME outer shell, an inherently ill-posed problem due to the scarce coronagraphic (2D) data available for any given event, see e.g., Mierla et al. (2009), Antunes, Thernisien, and Yahil (2009), Jackson et al. (2010), Mierla et al. (2010), Thernisien, Vourlidas, and Howard (2011), Joshi and Srivastava (2011), Feng, Inhester, and Mierla (2013), Cremades, Iglesias, and Merenda (2020), Sieyra et al. (2020), Verbeke et al. (2022). The 3D reconstruction with GCS is done in a manual and subjective way, by visually matching its 2D projections to coronagraphic images acquired quasi-simultaneously from 2 or 3 different vantage points, see e.g., Verbeke et al. (2022).

To isolate the CME signal from the background coronal emission, running-difference and base-difference techniques are usually applied to white-light coronagraphic images (Vourlidas et al. 2000, 2010). However, there are dynamic background coronal structures (e.g., streamers) that are not completely removed by difference techniques, particularly at lower heights close to the telescope's central occulter. To make the synthetic data more realistic,

we include these coronal structures in our synthetic training dataset by using as background actual running-difference coronagraphic images, which are manually checked to contain no CMEs (see Section 2.1). We employ data obtained by SoHO/LASCO C2, and SECCHI/COR2-A and B coronagraphs. Both instruments detect the Thomson scattering of photospheric light by free electrons in the solar corona (Billings 1966), with an effective field of view (FOV) of 2.2 – 6 $R_\odot$ and 2.5 – 15 $R_\odot$ for C2 and COR2, respectively.

2.1. Synthetic CME Dataset

Each element of the dataset used for training the DNN is composed of a synthetic coronagraphic image and its corresponding occulter and CME outer shell binary segmentation masks. This synthetic image represents a single running difference snapshot of a CME event, i.e. we produce only two time instants per event. The procedure used to obtain each element is outlined in Figure 3 and detailed below:

i) *Selection of background coronal image:* We manually select running-difference coronagraphic images that do not contain CMEs to use as background to our synthetic CMEs. In the first step, one background image (I_{back}) is randomly selected from the background pool. Our background pool has 213 images: 45, 39, and 129 from LASCO C2, COR2-A, and COR2-B, respectively, covering the minimum and rising phase of solar cycle 24 from the year 2007 to 2011. The standard Level 1 processing, made available in the SolarSoft library[7] by the respective instrument teams, is applied to the observations from the three coronagraphs. Subsequently, images are saved as binned, running-differences, with a size of 512×512 pixel^2.

ii) *Selection of GCS parameters:* We defined the following subspace of the GCS parameters based on CME statistical properties (see e.g., Cremades and Bothmer 2004; Vourlidas et al. 2017; Kay and Palmerio 2024):

$$\mathbf{P} = \{(-180, 180), (-70, 70), (-90, 90), (2.0, 20), (0.2, 0.6), (5, 65)\}. \quad (2)$$

This subspace is uniformly sampled using the Latin Hypercube method (McKay, Beckman, and Conover 1979), i.e., dividing the ranges in $\mathbf{P}$ by the desired size of the training dataset. Then, a point:

$$\mathbf{p_{e1}} = (\phi, \theta, \gamma, h, \kappa, \alpha), \quad (3)$$

is obtained by selecting a uniform random value from each GCS parameter in $\mathbf{P}$. From $\mathbf{p_{e1}}$, we derive three more sets of parameters to obtain two pairs, namely $\mathbf{p_{e0}}, \mathbf{p_{e1}}$ and $\mathbf{p_{c0}}, \mathbf{p_{c1}}$. Each pair is used to produce the differential image of the CME envelope and its core, respectively. The first pair models the outer envelope with parameters $\mathbf{p_{e1}}$ and a smaller envelope corresponding to a previous time with the parameters:

$$\mathbf{p_{e0}} = (F_0\phi, F_1\theta, F_2\gamma_0, h - F_3, F_4\kappa, F_5\alpha), \quad (4)$$

where F_0, F_1, and F_2 are uniform random numbers in the (0.95, 1.05) range, simulating the possible deflection and rotation of the CME, see e.g., Sieyra et al. (2020). F_3 is the CME displacement computed using a random velocity and assuming a cadence of 15 min (typical for the instruments used). The random velocity is derived from a log-normal random distribution with mean and standard deviation of log(433) and 0.5267,

[7] www.lmsal.com/solarsoft/.

respectively (Yurchyshyn et al. 2005), and forced to be in the (200, 1800) km s^{-1} range (Vourlidas et al. 2010). F_4 and F_5 are uniform random numbers in the (0.9, 1) range, simulating the non-self similar expansion of the CME, see e.g., Cremades, Iglesias, and Merenda (2020).

The second pair of GCS parameters is used to simulate the CME bright core, a conspicuous feature typically presented in CMEs and believed to generally lie at the bottom of a magnetic flux rope (Vourlidas et al. 2013). Their values are:

$$\mathbf{p_{c1}} = (\phi, \theta, \gamma, F_6 h, F_7 \kappa, \alpha) \tag{5}$$

and

$$\mathbf{p_{c0}} = (F_0\phi, F_1\theta, F_2\gamma, F_6 h - F_3, F_4 F_7 \kappa, F_5\alpha), \tag{6}$$

where F_6 is a uniform random number in the range (0.55, 0.85) or (0.45, 0.75) if h_0 is below or above 3 $R_\odot$, respectively, which controls the bright core height (Joshi and Srivastava 2011; Sarkar et al. 2019). F_7 is a uniform random number in the (0.2, 0.4) range, which defines the bright core smaller aspect ratio.

iii) *Generation of synthetic image*: We run the ray-tracing implementation by Thernisien, Vourlidas, and Howard (2009) in the four GCS models with parameters $\mathbf{p_{e1}}$, $\mathbf{p_{e0}}$, $\mathbf{p_{c1}}$ and $\mathbf{p_{c0}}$ to obtain four 512 × 512 pixel^2 corresponding synthetic images: I_{e1}, I_{e0}, I_{c1}, and I_{c0}. These images model the total brightness scattered by the CME outer envelope and bright core as observed from a given observer position, defined by [Carrington longitude, heliographic latitude, tilt with respect to the Solar North]. We use the fixed positions [300.082, 1.955, 0.000], [32.894, 7.051, 0.000], or [170.089, −6.587, 0.000] deg when using COR2-A, COR2-B or LASCO C2 background coronal images, respectively. The differential CME image is then obtained from:

$$I_{\rm cme} = F_{10}[I_{e1} - F_8 I_{e0} + F_9(I_{c1} - F_8 I_{c0})], \tag{7}$$

where $F_8 = (1 - F_3/h)^{-3}$ is a scaling factor based on the expected density reduction of an expanding CME given in Howard and Vourlidas (2018); F_9 is an ad-hoc uniform random number in the (0, 2) range that controls the relative levels of the differential CME bright core and outer envelope; and F_{10} is an ad-hoc random scaling map that varies smoothly in the (0.1, 1) range across the image. The latter is added to break the homogeneity of the brightness images produced by the ray-trace simulation of the simple and smooth GCS shape (which is far from the non-uniform brightness observed in real coronagraphic images).

The image $I_{\rm cme}$ is normalized to the (0, 1) range to obtain $\hat{I}_{\rm cme}$, and assemble the final output image as follows:

$$I = F_{11}\sigma(I_{\rm back})\hat{I}_{\rm cme} + I_{\rm back} + I_{\rm occ} + I_{\rm noise}, \tag{8}$$

where F_{11} is a uniform random number in the (2, 7) range and $\sigma(I_{\rm back})$ is the standard deviation of the background image. The product $F_{11}\sigma(I_{\rm back})$ is used to ensure the CME image is visible over differential backgrounds of varying contrasts, basically because the CME density assumed during the ray-tracing simulations is a constant number uncorrelated to the background coronal density that produced $I_{\rm back}$. The term $I_{\rm occ}$ is an artificial occulter of radius equal to the one present in $I_{\rm back}$ plus a random variation in the (1, 1.1) range, added to promote a more instrument independent response of the DNN. Finally, the term $I_{\rm noise}$ represents additive Poisson noise computed using $\hat{I}_{\rm cme}$.

iv) *Generation of binary segmentation masks:* We derive an outer envelope binary segmentation mask (M_{e1}) from I_{e1}, with value equal to one for all pixels in the interior of the geometrical border defined by the projection of $\mathbf{p_{e1}}$ and outside of the occulter, see Figure 3. We also obtain the central occulter binary mask $M_{\rm occ}$ from $I_{\rm occ}$. Given that we do an independent random sampling for each of the six GCS parameters in the subspace $\mathbf{P}$, there can be cases where the projected CME ($I_{\rm CME}$) lies only in the central area of the image occupied by the occulter, e.g., a small halo CME. These cases are eliminated from the dataset because M_{e1} is null. We also filter out any event that has M_{e1} fragmented by the occulter into two disconnected areas, e.g., in a halo CME of projected size similar to the occulter diameter. Note that we train Mask R-CNN to segment only the CME outer envelope, thus no mask is derived for the CME bright core ($\mathbf{p_{c1}}$ and $\mathbf{p_{c1}}$). This feature is added to the synthetic image to make the NN segmentation more robust against the strong intensity contrast typically observed in the interior of the CME envelope.

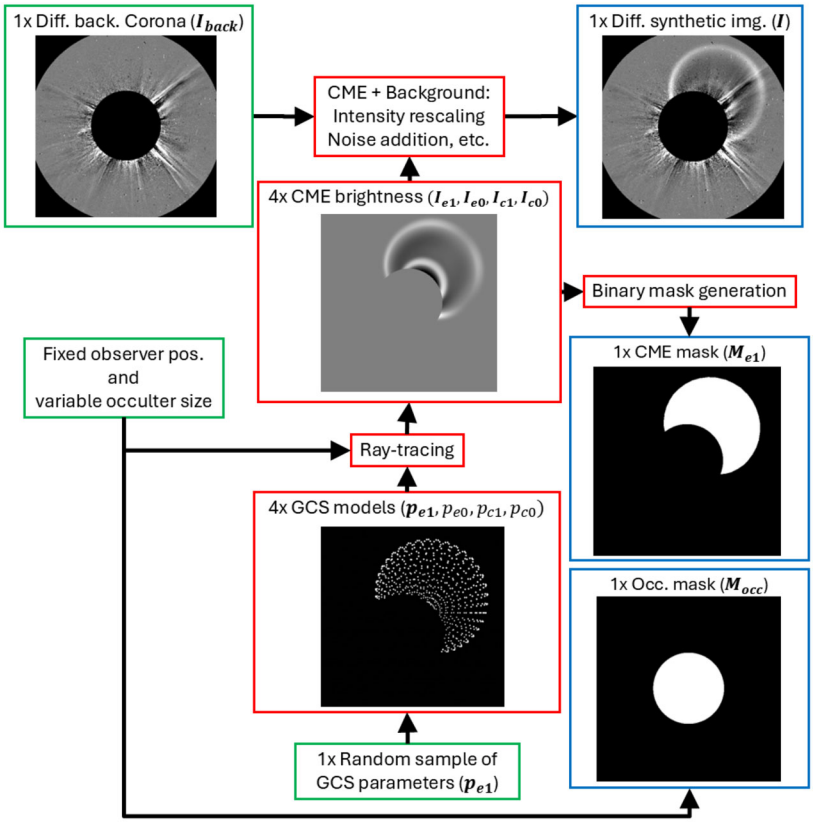


Figure 3 Generation of the empirical synthetic dataset. Each dataset element is composed of a differential synthetic coronograph image and its corresponding CME outer shell and occulter binary segmentation masks (blue boxes). These are produced using a real observed coronal background (with no CME) and synthetic brightness images obtained from a ray-tracing simulation based on a random GCS model (green boxes). The red boxes represent intermediate steps. Note that we show only one of the four GCS models for simplicity. We deliberately selected a case that highlights the main drawback of this approach, namely, the lack of correlation between CME and background structures. See the text for extra details.

The above-described procedure to generate synthetic images is based on the simple GCS model and includes various empirical parameters, thus presents the following main disadvantages:

- There is no correlation between the CME morphology and the background coronal structures, which is unrealistic. We deliberately chose an example that highlight this in Figure 3. For example, there are frequent observations of deflected streamers (e.g., Vourlidas et al. 2003; Vršnak et al. 2006; Tripathi and Raouafi 2007) or streamer blowouts (Sheeley et al. 1982; Vourlidas and Webb 2018) associated to CMEs, among others.
- We include an unrealistic random component of the CME brightness spatial variation that is not correlated with its morphology via F_{10}, see Eq. 7.
- The GCS gives a smooth geometric shape that is not representative of many real CMEs outer shells or bright cores, see e.g., Pluta et al. (2019), Verbeke et al. (2022).

And the following advantages:

- It can be used to efficiently generate as many synthetic images as necessary, to better investigate the training of large DNNs.
- By using a real observed coronal background (I_{back}), the dataset includes some of the complexity of the solar corona in different stages of the solar cycle.
- The desired properties of the output mask can be controlled based on the CME model used. For example, the GCS produces masks that are fully connected, and thus it is expected that the DNN learns to produce similar masks. This reduces the common issue of mixing CME and background fast moving material during segmentation of real observations, see Section 3.2.
- Our training dataset is public to help quantitatively compare the performance of different CME segmentation algorithms.[8]

We note that the above-named disadvantages are mostly related to the simplicity of the morphological and CME density models used. However, the approach presented in this work remains valid if a more accurate coronal and/or CME model is used to generate the synthetic images (see Section 4).

2.2. Neural CMEs Segmentation

2.2.1. Architecture and Supervised Training

We employ the PyTorch implementation of the Mask Region-based Convolutional Neural Network[9] (Mask R-CNN, He et al. 2017), which is a very successful DNN used for identifying and segmenting objects within images across various domains, including astronomy (Burke et al. 2019; Farias et al. 2020; Pearce-Casey et al. 2025). Mask R-CNN consists of three stages, see Figure 4. The first two stages are identical to those used in the precursor Faster R-CNN detector (Ren et al. 2015). The first stage, named Region Proposal Network, proposes candidate object bounding boxes. The second stage extracts features from each possible box and performs classification. The core of Mask R-CNN lies in the third stage, parallel to the second, that provides a mask for each region of interest. As backbone, we use the Residual Network (ResNet, He et al. 2015), which addresses the vanishing gradient problem when training very deep CNN by using residual connections. We employ a 50-layers

[8] See sites.google.com/um.edu.ar/gehme/science/cme-segmentation.

[9] Downloadable at docs.pytorch.org/vision/main/models/mask_rcnn.html.

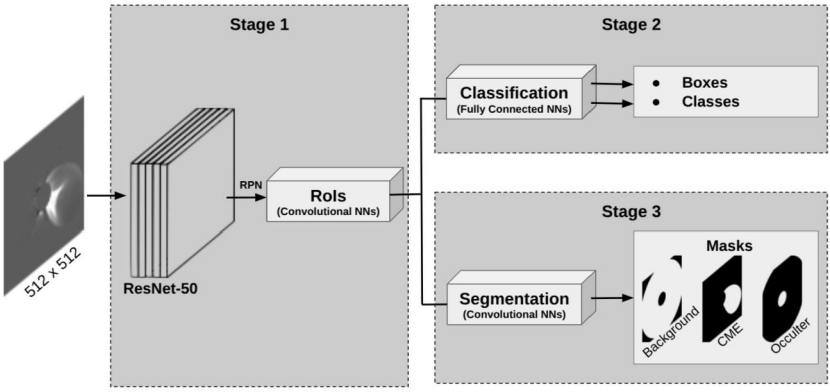


Figure 4 Architecture of the Mask R-CNN model (He et al. 2017) used for instance segmentation of CMEs in coronagraphic images. The backbone is a ResNet-50 with initial weights trained on the COCO dataset. We use the object classes: Background, CME and Occulter.

ResNet (Resnet-50) that has initial weights obtained by training it for image classification with the Common Objects in Context (COCO, Lin et al. 2014) dataset.

In our setup, the Mask R-CNN input is a single 512×512 pixel^2 differential coronagraphic image, while the outputs are the segmentation masks, class scores and bounding boxes the model found in the input. We apply a 3×3 pixel^2 median filter to reduce noise and then normalize the input images such that the range $[\mu_I - 2\sigma_I, \mu_I + 2\sigma_I]$ is mapped to $[0, 1]$. All pixels outside of this range are clipped. We define three object classes, two task-specific: *CME* and *Occulter*, and the *Background* required by the model. Each output mask is an array that gives for each pixel within the bounding box the inferred likelihood of the pixel belonging to the object (given by the class score). By thresholding each output mask (see Section 2.2.2), a corresponding binary segmentation mask can be derived ($\bar{M}^i_{e0}$). We use the upper index i to emphasize that Mask R-CNN is able to do instance segmentation, therefore multiple masks can be output for a single input image (see Section 2.2.3).

We generate a synthetic dataset of 1.13×10^5 images using the methodology described in Section 2.1. This dataset is split into 85% for training and 15% for validation. We train Mask R-CNN using a batch size of 20 images for 50 epochs, reaching a loss function of ≈ 0.5, see Figure 5 and He et al. (2017) for the exact definition of the loss. Given that in our synthetic dataset the true CME outer shell mask is known, we can quantify the error of each inferred mask by computing IoU between M_{e0} and each $\bar{M}^i_{e0}$, see Eq. 1.

2.2.2. Binary Segmentation Mask

We derive the final binary segmentation masks by defining a threshold such that all pixels in the Mask R-CNN output masks with values above the threshold are considered belonging to the object. In many applications, this mask threshold is typically in the $0.60 - 0.85$ range (e.g., López-Cano et al. 2024). We found that such large values lead to underestimations of the commonly diffuse and faint CME outer shell. We select a task-specific value via a simple hyperparameter search. For different values of the mask threshold, we compute the median IoU for 10^3 random synthetic validation images. We then selected the mask threshold value that maximizes such a validation IoU, see Figure 6. We obtain an optimal mask threshold value of 0.53, which is used for the rest of this work.

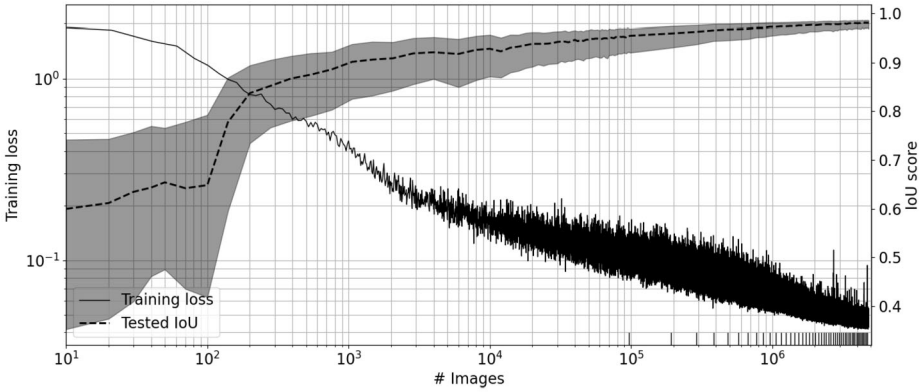


Figure 5 Mask R-CNN model training on synthetic coronagraphic images. We show the training loss (solid line) and mean validation IoU (dashed line, refer to the right vertical axis) as a function of the number of training images. The gray band represents the 25th-75th percentile of the IoU, which is computed for the validation set. Black vertical segments on the horizontal axis mark each training epoch.

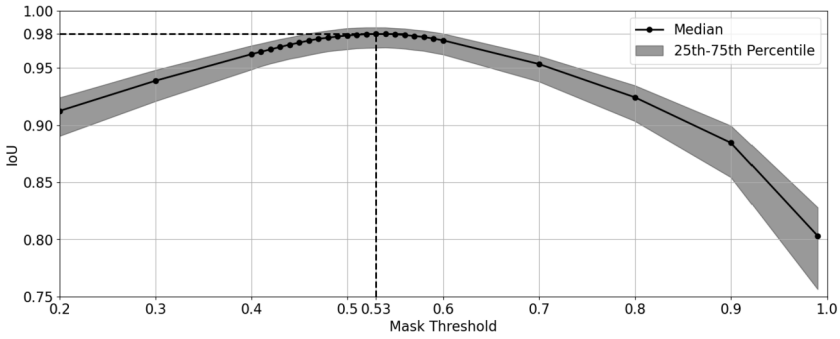


Figure 6 IoU versus mask threshold. The solid line and gray area indicate the median and 25th-75th percentiles of the IoU computed for 10^3 random images of the synthetic validation dataset. The dashed vertical and horizontal lines indicate the maximum.

2.2.3. Instance Selection via CME Tracking

Given that Mask R-CNN can perform instance segmentation, multiple CME masks can be produced for a single input image, including overlapping objects. This has the advantage that cases with multiple simultaneous CMEs can be identified, and the disadvantage of possible false positive detections. In other applications, this is typically addressed by keeping only outputs with class scores larger than a predefined threshold, after possibly eliminating overlapping objects using IoU. However, we found that this approach cannot be consistently used to select the best CME mask, particularly in cases of very faint and diffuse borders, nor to differentiate a false positive detection from the correct detections in images of multiple CMEs events. Another approach, applicable when a time series of a CME event is available, is to use the expected temporal behavior of CME mask properties to select the correct instance. This is the CME tracking step included in all methods shown in Figure 1. The main difference is that the other techniques use this step to eliminate undesired portions of the mask(s), altering their final shape. On the contrary, we use CME tracking only to select the

best of the multiple masks found in each input image. The procedure, similar to that given in Shan et al. (2024) but simpler, is outlined below.

We start with a time series of M differential images of a CME event. For each image, our trained Mask R-CNN infers (possibly) multiple CME binary masks. By selecting one mask per image, we obtain a specific temporal sequence of masks. Firstly, we compute all the possible sequences in the time series, the goal is to find the sequence that best resembles a radially propagating CME. Secondly, we compute the apex (percentile 98 of the radial distance distribution of the mask pixels) of all the masks in each sequence. Each sequence that includes two temporally consecutive masks with apex difference smaller than that corresponding to a radial growth of 200 km s^{-1} (lowest yearly average radial speed, proxy value from Vourlidas et al. 2017) is eliminated. Thirdly, we compute for each sequence a total error, which quantifies the similarity of the masks. The error between the consecutive masks number n and $n+1$ in a sequence is:

$$\Delta_n = \omega_{\mathrm{CPA}} \cdot \Delta_{\mathrm{CPA}} + \omega_{\mathrm{AW}} \cdot \Delta_{\mathrm{AW}} + \omega_{IoU} \cdot \Delta_{IoU}, \tag{9}$$

where Δ_{CPA} and Δ_{AW} are the differences of the masks Central Position Angles (CPAs) and Angular Widths (AWs), respectively. The CPA and AW of each mask are defined as the median, and the difference between percentile 95 and 5, of the position angles distribution, respectively. Δ_{IoU} is the inverse of the IoU between the masks, and the ω are normalization constants used to keep each term of the sum in the 0-1 range. Finally, the mask sequence that minimizes the total error, $\sum_{n=1}^{M} \Delta_n$, is selected.

3. Results and Discussion

3.1. Performance on Synthetic Validation Data

Figure 5 presents IoU computed for 10^3 random images of the synthetic validation dataset, at different stages during training. This is computed using the optimal mask threshold of Section 2.2.2 and, for each image, using only the output mask that best matches M_{e0}. Due to the latter, this IoU does not measure false positive masks, while it is sensitive to false positive pixels within the selected mask. It can be seen that the initial IoU is ≈ 0.6, which corresponds to the ResNet backbone pretrained on the COCO dataset (with no CME images). We also show in Figure 7 the relationship between IoU and the more intuitive RSD. Note that RSD simply measures the non-overlapping area relative to the true mask area, thus depends on the true mask size. For good performance, namely $IoU > 0.8$ and $RSD < 20\%$, the relationship is practically linear ($IoU = 1 - RSD$). For poor performance, there can be cases with $RSD > 1$ if the total non-overleaping area is larger than the true mask area, see Eq. 1 and more details below in Section 3.2. The initial and final validation IoU found during training, 0.6 and 0.98, correspond to $RSD \approx 40 - 65\%$ and $\approx 2\%$, respectively. The median obtained with the trained Mask R-CNN on 1.6×10^4 validation images is 0.98, with 88% (1.4×10^4) of the masks having $IoU \geq 0.95$ or $RSD \leq 5\%$. In Figure 8, we present examples of detected masks along with the corresponding true mask for six values of IoU, ranging from poor to excellent. Note that we only show the outline of the masks because they do not present holes or isolated patches.

The variety of GCS shapes included in the synthetic dataset allows to study the performance of the detection with respect to various CME properties. Figure 9 presents the apex, AW and CPA of the true and inferred masks for the 1.6×10^4 synthetic validation images.

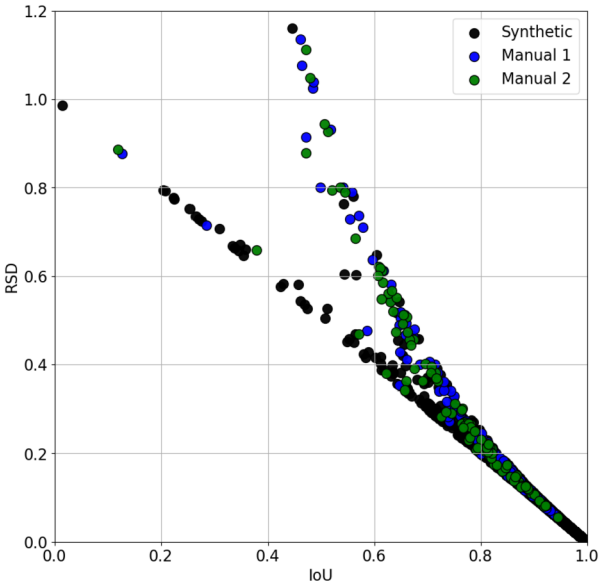


Figure 7 RSD vs IoU, refer to Eq. 1, computed for 1.6×10^4 synthetic validation images (*black points*) and 115 CME observations manually segmented by two independent operators (*blue and green points*).

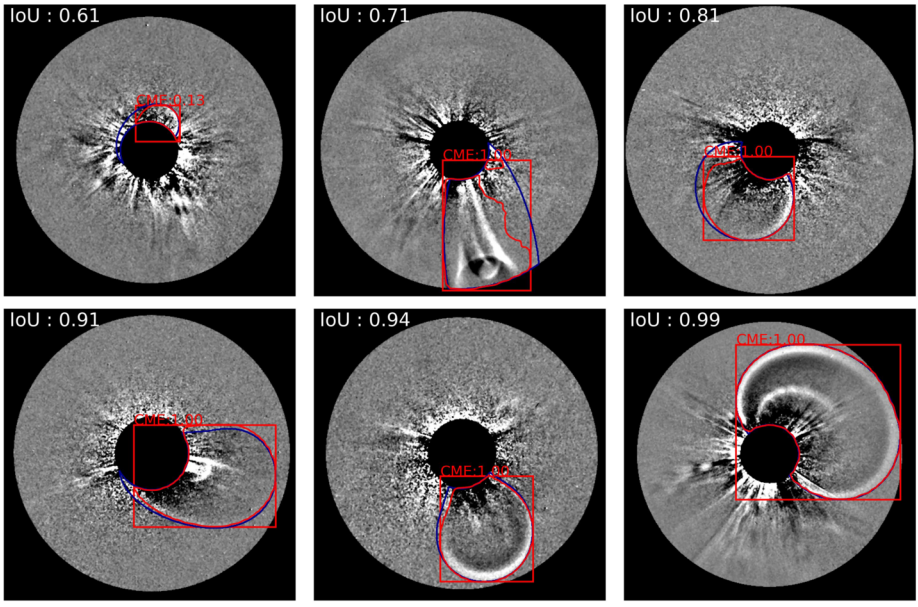


Figure 8 CME outer shell segmentation in synthetic validation images (*red contour*) in comparison with the known true mask (*blue contour*) for six values of IoU, ranging from poor (*top left panel*) to excellent (*bottom right panel*). Note that we only show the outlines of the masks and they may partially overlap.

It can be seen that the agreement is better for apex and CPA than for AW, because the latter is very sensitive to the detailed mask shape near the occulter. The AW result suggests that the performance is worse for narrow than wide, halo-like CMEs. The median IoU for CMEs with AW $< 30°$ (122 cases) and $> 300°$ (132 cases) are 0.90 and 0.94, respectively.

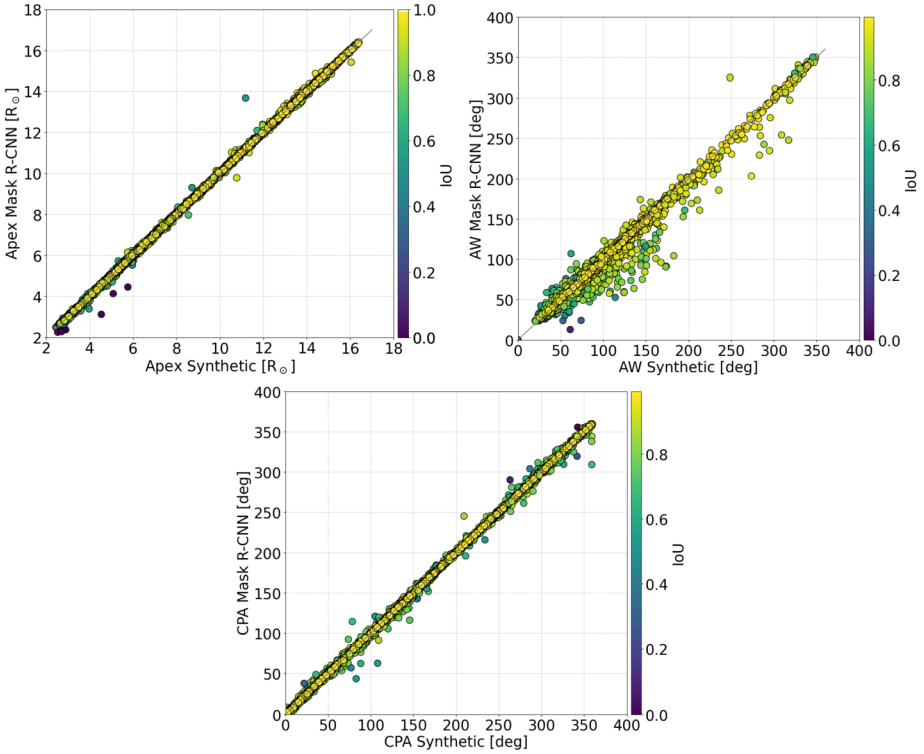


Figure 9 Apex (*top left*), AW (*top right*) and CPA (*bottom*) of the true masks (*horizontal axes*) for 1.6×10^4 synthetic validation images, versus the values for the masks obtained with our trained Mask R-CNN (*vertical axes*). The color bar indicates the IoU score of each image. The solid lines have slope one.

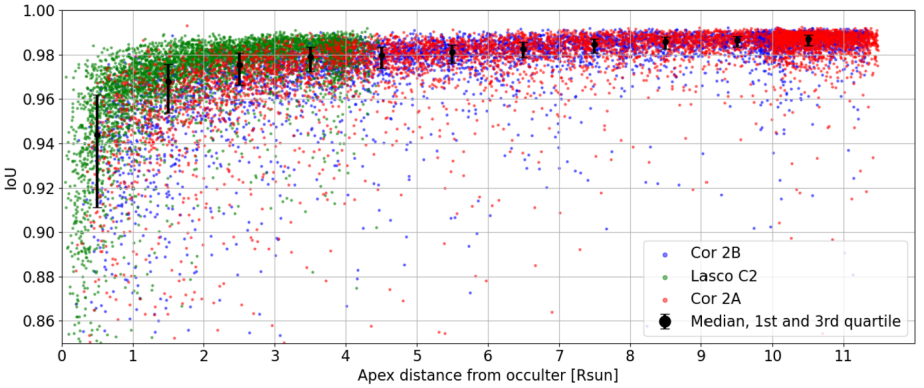


Figure 10 IoU versus CME apex measured from the occulter for 1.6×10^4 validation synthetic images. LASCO C2 and COR2-A/B are indicated as green, red, and blue colors, respectively. Black dots and error bars indicate the median and 25th – 75th percentiles for all cases in centered bins of size ± 0.5 $R_\odot$.

To study the variation of the inferred mask accuracy with respect to the CME height, we present in Figure 10 the IoU versus CME apex, as measured from the occulter. It can be seen that for lower heights the median detection quality and the spread degrade, with the

lowest quartile going from $IoU \approx 0.98$ ($RSD \approx 2\%$) to $IoU \approx 0.91$ ($RSD \approx 9\%$). We associate this reduction to the increased contrast of the background coronal structures. Note that there can still be good detections at lower heights if the CME is well defined, namely it has a large differential signal with respect to the background. More importantly, this dependence is similar in all three instruments, even when their occulters have different radii, namely 1.7 and 2.5 $R_\odot$ for C2 and COR2, respectively. This suggests the relevant factor is related to the coronograph stray light rejection performance, which dominates the contrast near the occulter, over the intrinsic coronal structures.

3.2. Performance on CME Observations

Mask R-CNN can identify multiple instances of the CME class. When applied to coronagraphic observations, this improves the detection of multiple CMEs in a single differential image, even when CMEs are close to each other (see Figure 11), and reduces the false detection of fast moving background material. The latter is particularly challenging to achieve using traditional segmentation algorithms or other neural methods, which do not incorporate morphological constraints. For example, Figure 12 shows the segmentations obtained by our method and by Shan et al. (2024) as presented in their public catalog.[10] Note that our

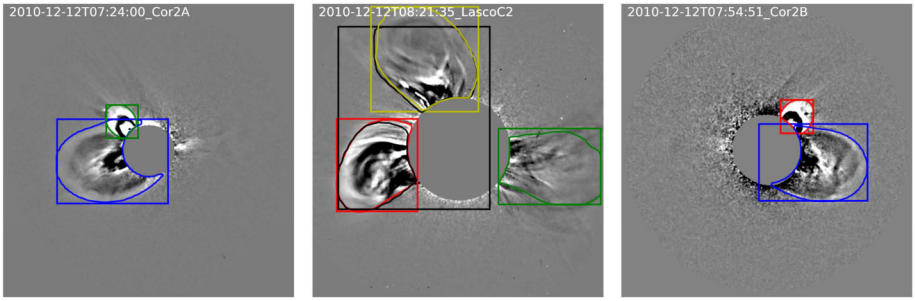


Figure 11 Segmentation of multiple CMEs observed by COR2-A (*left*), LASCO C2 (*middle*) and COR2-B (*right*). The outlines of all mask instances found by our trained Mask R-CNN in each image independently are shown in different colors. Note that some outlines partially overlap.

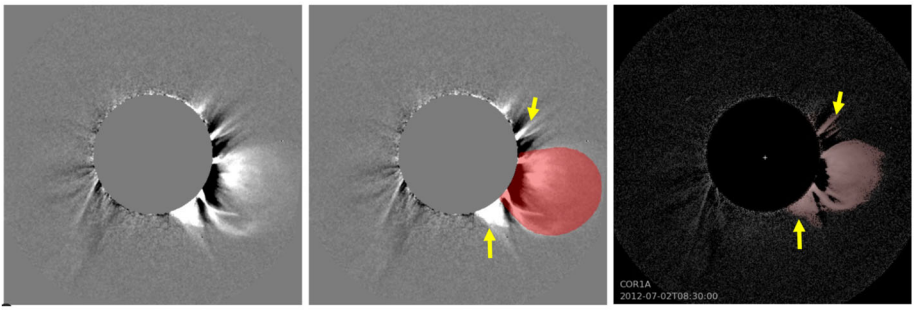


Figure 12 Segmentation comparison for the CME observed by COR1-A on 2012/07/02 at 08:30:00 (*left*). Note that our model-based approach *(middle)* produces simpler shapes than Shan et al. (2024) *(right)*, but is able to better distinguish between the main CME bulk and nearby fast moving material (*yellow arrows*).

[10] Available at aso-s.pmo.ac.cn/feature/#/CME_2d_catalog.

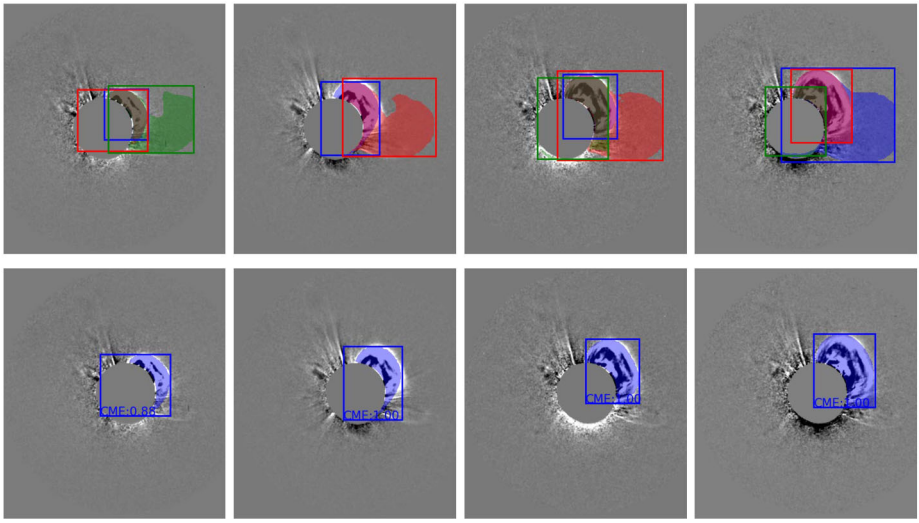


Figure 13 Mask instance selection by CME tracking. We show in different colors all the masks found by Mask R-CNN (*panels in the top row*) for the CME observed by Cor2A on 2011/06/05 at 07:54:25, 08:24:25, 08:39:25 and 08:54:25 (*from left to right*). The selected masks are given in blue in the bottom row panels.

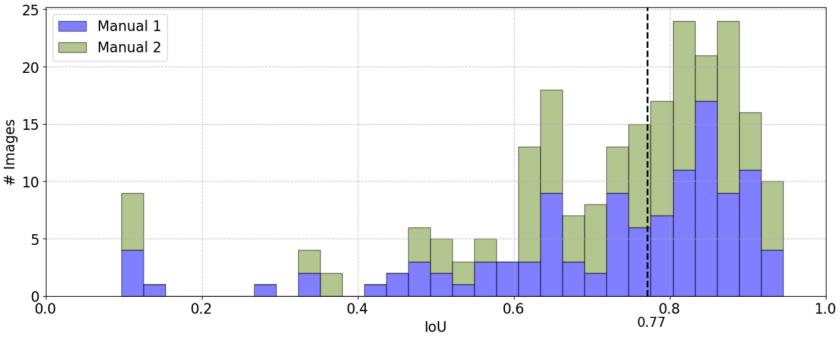


Figure 14 Histogram of IoU between masks inferred by our method and manual operators 1 (*blue*) and 2 (*green*), for 115 CME observations acquired by COR2-A, COR2-B and LASCO C2. The dashed vertical line indicates the overall median. See the text for extra details.

model-based training approach produces simpler shapes, which may not be representative of complex CMEs, but can better distinguish between the main CME bulk and other fast moving material based only on their morphology, i.e., with no further kinematic information.

If the time series of images for a CME event is available, the expected temporal variation of basic CME morphological properties can be used to select one of the multiple inferred masks in each image, minimizing false positive masks. The result of applying the procedure described in Section 2.2.3 is shown in Figure 13.

To quantify the performance of our instance segmentation, we apply it to 115 images corresponding to the CME events listed in Cremades, Iglesias, and Merenda (2020), and compare the results with masks derived manually. These are images of 12 CME events acquired at different instants and from three different vantage points, by LASCO, COR2-A,

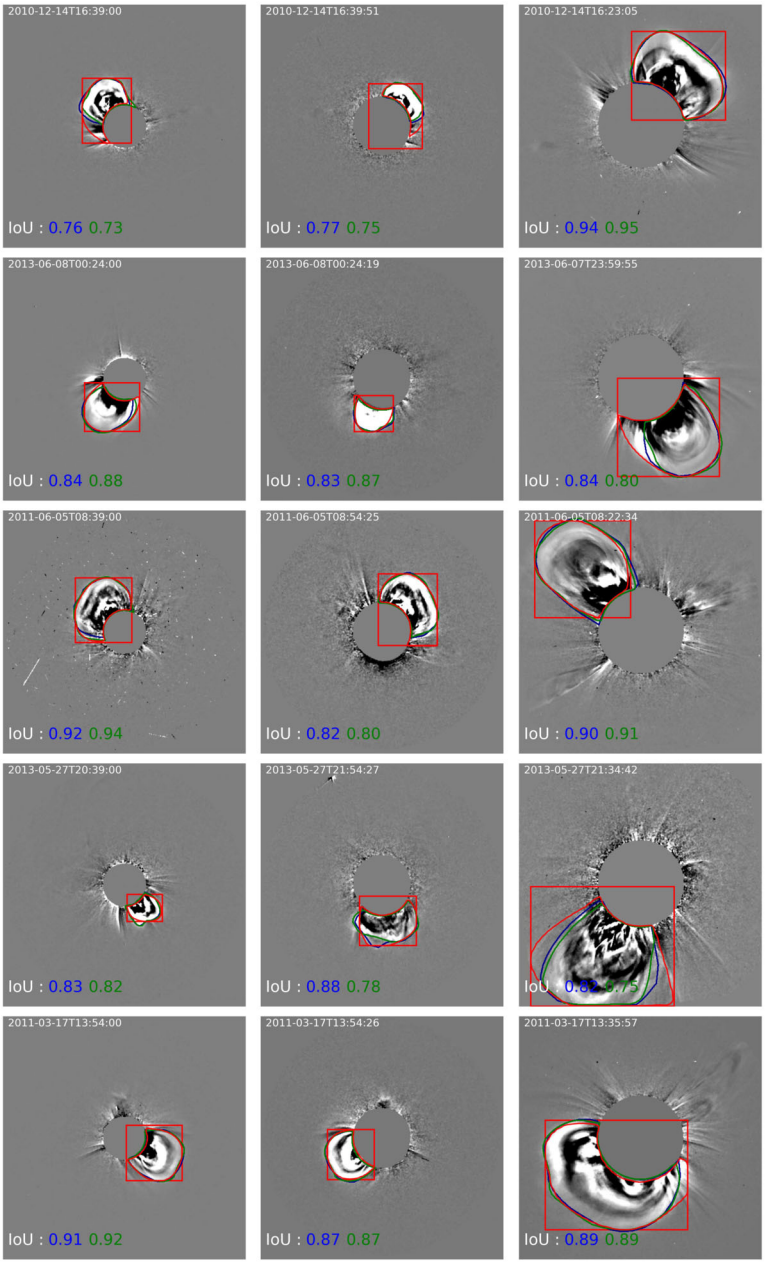


Figure 15 CME outer shell segmentation using our method (*red contour*) versus independent manual estimations by operator 1 (*blue contour*) and 2 (*green contour*). The observations were acquired by COR2-A (*leftmost column*), COR2-B (*middle column*) and LASCO C2 (*rightmost column*). We show cases with $IoU \geq 0.75$ between inferred and manual masks, as annotated in the images. See the text for extra details.

and COR2-B. These events have CPA within 25° of the solar poles, to minimize projection effects, and have AWs $\geq 20°$, therefore, not jet-like or halo CME are included. For more de-

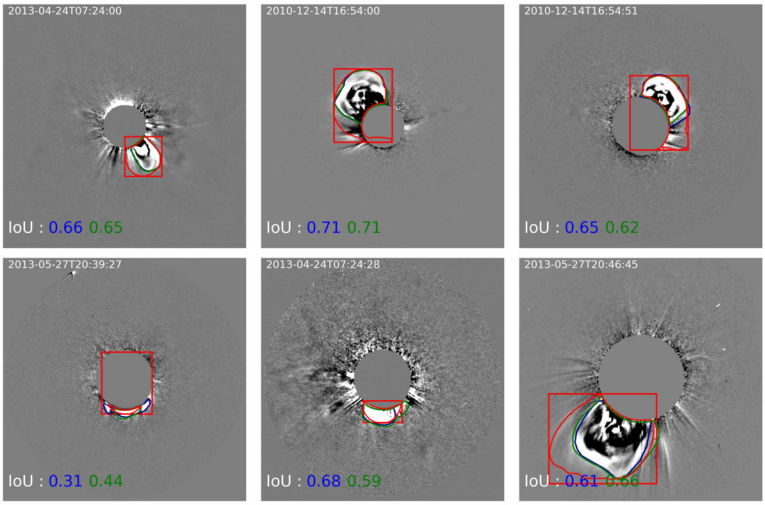


Figure 16 Same as Figure 15 but for cases with $IoU < 0.75$. The observations were acquired by COR2-A (*panels 1 – 2*), COR2-B (*panels 3 – 5*) and LASCO C2 (*last panel*). See the text for extra details.

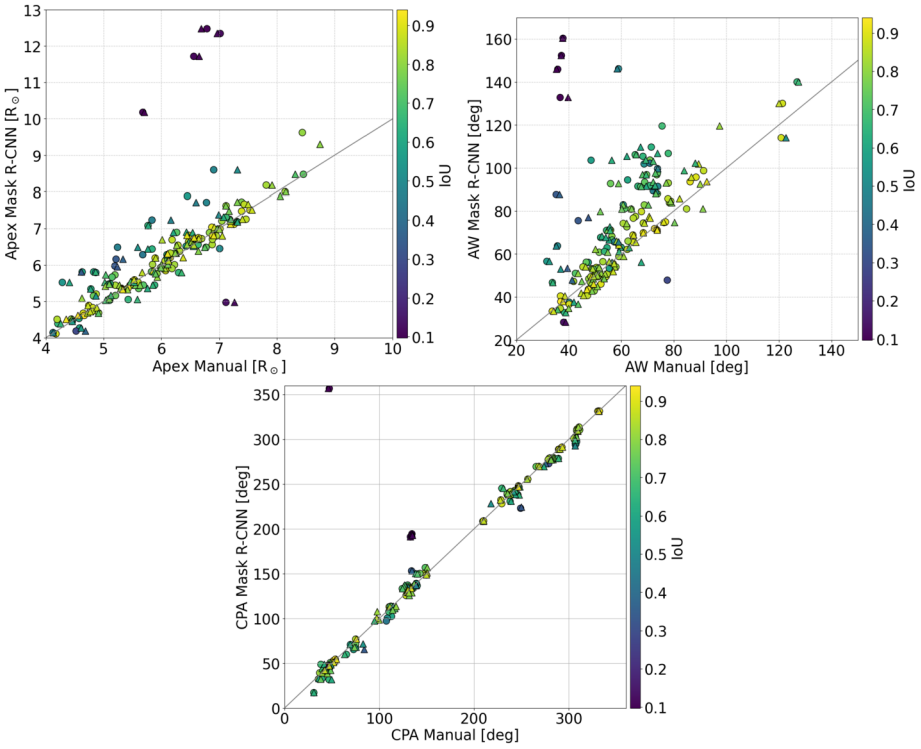


Figure 17 Apex (*top left*), AW (*top right*) and CPA (*bottom*) of the masks obtained with our trained Mask R-CNN (*vertical axes*) and manually (*horizontal axes*). We separate the results of manual operator 1 (*triangles*) and 2 (*squares*). The color bar indicates the IoU score of each image. The solid lines have slope one.

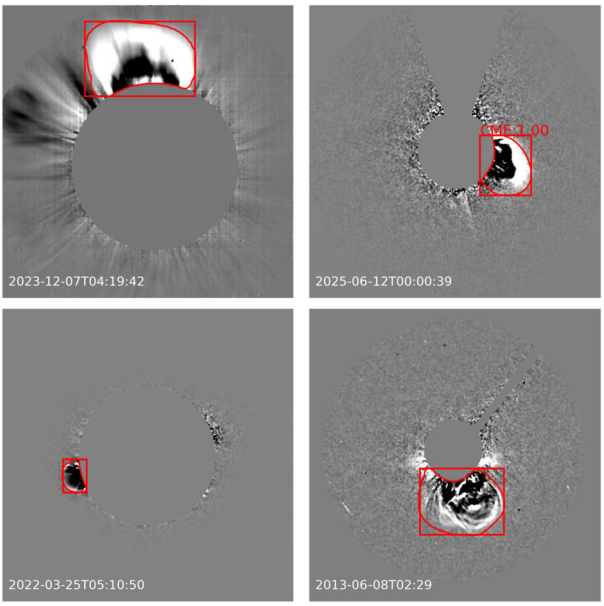


Figure 18 CME segmentation for instruments not included in the Mask R-CNN training dataset. From *left* to *right* and *top* to *bottom*, we show observations by Metis (visible light) onboard Solar Orbiter; by CCOR-1/GOES-19 where we masked out the occulter pylon, by the Full Sun Imager onboard Solar Orbiter at 17.4 nm, where we masked out the solar disk; and by LASCO C3 onboard SoHO.

tails on the events see Cremades, Iglesias, and Merenda (2020). The manual segmentations are produced by two independent expert operators by manually selecting points outlying the CME outer envelope. A binary segmentation mask is derived from the selected points using second-order polygons. The histogram of the resulting IoU is shown in Figure 14, which indicates that the median IoU is 0.77 ($RSD \approx 20-25\%$). As a reference, when comparing the masks of the manual segmentations by operator 1 with operator 2, the median $IoU = 0.90$. Examples of good ($IoU \geq 0.75$) and bad ($IoU \leq 0.75$) segmentations are given in Figure 15 and Figure 16, respectively. We note that in many incorrect segmentations, Mask R-CNN treats nearby structures as part of the CME bulk, an aspect that could be improved by including kinematic information (see Section 4). Additionally, it is worth noting that in some of the Figure 16 cases, there is substantial disagreement even among the independent operators that performed the manual segmentation.

To link the mask overlapping metrics (IoU and RSD) with simpler and commonly used morphological properties, we plot in Figure 17 the relation between the apex, AW, and CPA of the manual and inferred masks. Excluding cases with $IoU < 0.3$, which are few (4.8%), the best Pearson correlation coefficient is found for CPA (0.99), followed by apex (0.91) and AW (0.77). The latter two are more dependent on the mask shape, thus they can differ even in cases of segmentations with good area overlapping ($IoU \geq 0.75$). The overestimation of AW by the DNN in cases with IoU between 0.5 and 0.8 is mostly explained by the fact that the DNN mask may overestimate the CME envelope in regions near the occulter, due to the low signal-to-noise ratio. The overestimation of the apex is more frequent in cases when the outer envelope is faint or when the part of the CME leading shock is wrongly captured.

The performance of our method on observations acquired by the instruments included in the training backgrounds (LASCO C2 and COR2-A/B) is demonstrated in Figures 11 to 17. A significant finding, however, is the generalization capability of our trained Mask R-CNN when applied to observations from other instruments with distinct fields of view, spatial resolutions, and stray light rejection performance, among others. Even though we do not perform a general quantitative analysis, Figure 18 exemplifies the segmentations obtained

for CMEs observed by Metis (Antonucci et al. 2020; De Leo et al. 2023) onboard Solar Orbiter, by the Compact Coronagraphs for the Geostationary Operational Environmental Satellite-19 (CCOR-1/GOES-19, Thernisien et al. 2025), by the Full Sun Imager 17.4 nm (Extreme Ultraviolet Imager, Rochus et al. 2020) onboard Solar Orbiter, and by LASCO C3 (Morrill et al. 2006) onboard SoHO.

4. Conclusions and Outlook

We developed a synthetic dataset of CME differential coronagraphic images, and used it to train the commercial-off-the-shelf neural model Mask R-CNN, to perform instance segmentation of the CME outer envelope. Our dataset is generated using an empirical approach that combines coronagraphic observations of the solar corona, with no CME, and synthetic brightness images obtained using a simple CME morphological model, the GCS, and ray-tracing. We have estimated the performance on synthetic validation images, obtaining a median $IoU = 0.98$ ($RSD = 2\%$), and on manually segmented CME observations acquired by LASCO C2 and COR2-A/B coronagraphs, reaching a median $IoU = 0.77$ ($RSD = 20-30\%$). The model-driven synthetic training allows Mask R-CNN to produce GCS-like (not strictly) masks. These masks are smooth and not representative of the complex exact shape of many CME outer shells. However, they are topologically connected (no holes or isolated patches), which helps to reduce mixing CME bulk material with nearby fast moving structures and segment multiple nearby CMEs, even when no kinematic information is used (other than that given by the single input differential image). Future aspects worth of further investigation include:

- We consider that an important improvement of the segmentation can be done by incorporating kinematic information. Namely, by selecting a DNN architecture that can process the whole time series of an event simultaneously, similar to Bauer et al. (2025).
- Combine our approach with other neural techniques that can produce more detailed segmentation masks, such as Shan et al. (2024) and Lin et al. (2024), to improve their mask filtering step and better reject moving features that are not part of the CME.
- We are currently developing a k-means based clustering method to allow the CME tracking procedure (Section 2.2.3) to detect the temporal sequence of simultaneous multiple CMEs.
- Producing a catalog of segmented CMEs from large observational databases that include faint and narrow events, such as those from SoHO/LASCO and STEREO/CORs, to systematically evaluate performance with respect to manual (CDAW), image processing (CORSET) and, particularly, other neural (Shan et al. 2024; Lin et al. 2024) techniques.

Our trained Mask R-CNN also shows an interesting generalization when applied to observations from other instruments with very different properties, including fields of view, spatial resolutions, and stray light rejection performance, among others. This generalization capability is a desired property for any automatic detection tool. Particularly for onboard operation in space platforms, where autonomous identification and prioritization of images is required to exploit the limited telemetry.

We finally note that the same technique presented in this work can be used with more realistic CME and/or coronal numerical models to produce the synthetic images, while preserving the desired morphological properties of the masks. Notable candidates are 3D magnetohydrodynamic (MHD) CME simulations, such as the Alfvén Wave Solar model

(AWSoM, Sokolov et al. 2013; van der Holst et al. 2014), that can include flux rope parameters produced by the Eruptive Event Generator based on Gibson-Low (EEGGL, Borovikov et al. 2017) to initiate the CME simulation; or the coronal 3D MHD model COolfluid COro-Nal UnsTructured (COCONUT, Wang et al. 2022) that can use a Titov-Démoulin flux rope (Titov et al. 2014) to initiate the CME simulation. These MHD models could allow defining the CME boundary not only based on brightness spatio-temporal variations, but also on other relevant physical variables, such as density or velocity gradients.

Acknowledgments Authors acknowledge use of data from the STEREO (NASA) and SOHO (ESA/NASA) missions, produced by the SECCHI and LASCO international consortia. Solar Orbiter is a mission of international cooperation between ESA and NASA, operated by ESA. Metis was built and operated with funding from the Italian Space Agency (ASI), under contracts to the National Institute of Astrophysics (INAF) and industrial partners. Metis was built with hardware contributions from Germany (Bundesministerium für Wirtschaft und Energie through DLR), from the Czech Republic (PRODEX) and from ESA. The EUI instrument was built by CSL, IAS, MPS, MSSL/UCL, PMOD/WRC, ROB, LCF/IO with funding from the Belgian Federal Science Policy Office (BELSPO/PRODEX PEA 4000112292); the Centre National d'Etudes Spatiales (CNES); the UK Space Agency (UKSA); the Bundesministerium für Wirtschaft und Energie (BMWi) through the Deutsches Zentrum für Luft- und Raumfahrt (DLR); and the Swiss Space Office (SSO). The Compact Coronagraph-1 (CCOR-1) instrument was designed, built, and tested by the U.S. Naval Research Laboratory (NRL) and is part of NOAA's Space Weather Follow-On (SWFO) Program.

Author Contributions FAI and DGL contributed equally to this work and should be considered first authors. FAI, DGL, FLC, MST, and YM implemented the software pipeline to generate the synthetic dataset and to train and evaluate the Mask R-CNN model. HC and FML preprocessed the CME observations and performed the manual segmentations used as ground truth for evaluation. FAI drafted the manuscript. DGL prepared all figures except Figures 1 and 3 (prepared by FAI), Figure 2 (prepared by FM), Figures 4 and 12 (prepared by YM), and Figure 13 (prepared by FLC). All authors contributed to developing the technique, evaluating its performance, reviewing and revising the manuscript, and approved the final version.

Funding Information FAI, HC and FML are members of the "Carrera del Investigador Científico" of CONICET. DGL and FM were supported by CONICET scholarships. FAI, FLC and MST are supported by The Max Planck Partner Group between the University of Mendoza and the Max Planck Institute for Solar System Research (MPS). This research is sponsored by the Department of the Navy, Office of Naval Research Global, under Grant Award number N629092512017. Any opinions, findings, and conclusions or recommendations expressed in this material are those of the authors and do not necessarily reflect the views of the Office of Naval Research. This work is also part of the DynaSun project and has thus received funding under the Horizon Europe programme of the European Union under grant agreement no. 101131534. Views and opinions expressed are however those of the authors only and do not necessarily reflect those of the European Union and therefore the European Union cannot be held responsible for them.

Data Availability The training synthetic dataset created and used in this project for the DNN training is publicly available on https://sites.google.com/um.edu.ar/gehme/science/cme-segmentation.

Declarations

Competing Interests The authors declare no competing interests.

Open Access This article is licensed under a Creative Commons Attribution-NonCommercial-NoDerivatives 4.0 International License, which permits any non-commercial use, sharing, distribution and reproduction in any medium or format, as long as you give appropriate credit to the original author(s) and the source, provide a link to the Creative Commons licence, and indicate if you modified the licensed material. You do not have permission under this licence to share adapted material derived from this article or parts of it. The images or other third party material in this article are included in the article's Creative Commons licence, unless indicated otherwise in a credit line to the material. If material is not included in the article's Creative Commons licence and your intended use is not permitted by statutory regulation or exceeds the permitted use, you will need to obtain permission directly from the copyright holder. To view a copy of this licence, visit http://creativecommons.org/licenses/by-nc-nd/4.0/.

References

Alshehhi, R., Marpu, P.R.: 2021, Detection of coronal mass ejections using unsupervised deep clustering. *Sol. Phys.* **296**(6), 104. DOI. ADS.

Antonucci, E., Romoli, M., Andretta, V., Fineschi, S., Heinzel, P., Moses, J.D., Naletto, G., Nicolini, G., Spadaro, D., Teriaca, L., Berlicki, A., Capobianco, G., Crescenzio, G., Da Deppo, V., Focardi, M., Frassetto, F., Heerlein, K., Landini, F., Magli, E., Marco Malvezzi, A., Massone, G., Melich, R., Nicolosi, P., Noci, G., Pancrazzi, M., Pelizzo, M.G., Poletto, L., Sasso, C., Schühle, U., Solanki, S.K., Strachan, L., Susino, R., Tondello, G., Uslenghi, M., Woch, J., Abbo, L., Bemporad, A., Casti, M., Dolei, S., Grimani, C., Messerotti, M., Ricci, M., Straus, T., Telloni, D., Zuppella, P., Auchère, F., Bruno, R., Ciaravella, A., Corso, A.J., Alvarez Copano, M., Aznar Cuadrado, R., D'Amicis, R., Enge, R., Gravina, A., Jejčič, S., Lamy, P., Lanzafame, A., Meierdierks, T., Papagiannaki, I., Peter, H., Fernandez Rico, G., Giday Sertsu, M., Staub, J., Tsinganos, K., Velli, M., Ventura, R., Verroi, E., Vial, J.-C., Vives, S., Volpicelli, A., Werner, S., Zerr, A., Negri, B., Castronuovo, M., Gabrielli, A., Bertacin, R., Carpentiero, R., Natalucci, S., Marliani, F., Cesa, M., Laget, P., Morea, D., Pieraccini, S., Radaelli, P., Sandri, P., Sarra, P., Cesare, S., Del Forno, F., Massa, E., Montabone, M., Mottini, S., Quattropani, D., Schillaci, T., Boccardo, R., Brando, R., Pandi, A., Baietto, C., Bertone, R., Alvarez-Herrero, A., García Parejo, P., Cebollero, M., Amoruso, M., Centonze, V.: 2020, Metis: the Solar Orbiter visible light and ultraviolet coronal imager. *Astron. Astrophys.* **642**, A10. DOI. ADS.

Antunes, A., Thernisien, A., Yahil, A.: 2009, Hybrid reconstruction to derive 3D height – time evolution for coronal mass ejections. *Sol. Phys.* **259**, 199. DOI. ADS.

Asensio Ramos, A., Requerey, I.S., Vitas, N.: 2017, DeepVel: deep learning for the estimation of horizontal velocities at the solar surface. *Astron. Astrophys.* **604**, A11. DOI. ADS.

Asensio Ramos, A., Cheung, M.C.M., Chifu, I., Gafeira, R.: 2023, Machine learning in solar physics. *Living Rev. Sol. Phys.* **20**(1), 4. DOI. ADS.

Bauer, M., Le Louëdec, J., Amerstorfer, T., Barnard, L., Barnes, D., Lammer, H.: 2025, Solar transient recognition using deep learning (strudl) for heliospheric imager data. *Space Weather* **23**(9), e2025SW004561. DOI. https://agupubs.onlinelibrary.wiley.com/doi/abs/10.1029/2025SW004561.

Billings, D.E.: 1966, *A Guide to the Solar Corona*, Elsevier Science, New York. ADS.

Borovikov, D., Sokolov, I.V., Manchester, W.B., Jin, M., Gombosi, T.I.: 2017, Eruptive event generator based on the Gibson-Low magnetic configuration. *J. Geophys. Res. Space Phys.* **122**(8), 7979. DOI. ADS.

Boursier, Y., Lamy, P., Llebaria, A., Goudail, F., Robelus, S.: 2009, The ARTEMIS catalog of LASCO coronal mass ejections. Automatic recognition of transient events and Marseille inventory from synoptic maps. *Sol. Phys.* **257**, 125. DOI.

Brueckner, G.E., Howard, R.A., Koomen, M.J., Korendyke, C.M., Michels, D.J., Moses, J.D., Socker, D.G., Dere, K.P., Lamy, P.L., Llebaria, A., Bout, M.V., Schwenn, R., Simnett, G.M., Bedford, D.K., Eyles, C.J.: 1995, The Large Angle Spectroscopic Coronagraph (LASCO). *Sol. Phys.* **162**, 357. DOI.

Burke, C.J., Aleo, P.D., Chen, Y.-C., Liu, X., Peterson, J.R., Sembroski, G.H., Lin, J.Y.-Y.: 2019, Deblending and classifying astronomical sources with Mask R-CNN deep learning. *Mon. Not. R. Astron. Soc.* **490**(3), 3952. DOI. ADS.

Byrne, J.P., Morgan, H., Habbal, S.R., Gallagher, P.T.: 2012, Automatic detection and tracking of coronal mass ejections. II. Multiscale filtering of coronagraph images. *Astrophys. J.* **752**, 145. DOI.

Camporeale, E.: 2019, The challenge of machine learning in space weather: nowcasting and forecasting. *Space Weather* **17**(8), 1166. DOI. ADS.

Chaumette, F.: 2004, Image moments: a general and useful set of features for visual servoing. *IEEE Trans. Robot.* **20**(4), 713. DOI.

Cremades, H., Bothmer, V.: 2004, On the three-dimensional configuration of coronal mass ejections. *Astron. Astrophys.* **422**, 307. DOI.

Cremades, H., Iglesias, F.A., Merenda, L.A.: 2020, Asymmetric expansion of coronal mass ejections in the low corona. *Astron. Astrophys.* **635**, A100. DOI. ADS.

De Leo, Y., Burtovoi, A., Teriaca, L., Romoli, M., Chioetto, P., Andretta, V., Uslenghi, M., Landini, F., Susino, R., Pancrazzi, M., Frassati, F., Giarrusso, M., Giordano, S., Zangrilli, L., Spadaro, D., Abbo, L., Bemporad, A., Capobianco, G., Capuano, G.E., Casini, C., Casti, M., Corso, A.J., Da Deppo, V., Fabi, M., Fineschi, S., Frassetto, F., Grimani, C., Guglielmino, S.L., Heinzel, P., Jerse, G., Liberatore, A., Magli, E., Massone, G., Messerotti, M., Moses, J.D., Naletto, G., Nicolini, G., Pelizzo, M.G., Romano, P., Russano, G., Sasso, C., Schühle, U., Straus, T., Slemer, A., Stangalini, M., Telloni, D., Volpicelli, C.A., Zuppella, P.: 2023, In-flight radiometric calibration of the Metis Visible Light channel using stars and comparison with STEREO-A/COR2 data. *Astron. Astrophys.* **676**, A45. DOI. ADS.

Deng, J., Dong, W., Socher, R., Li, L.-J., Li, K., Fei-Fei, L.: 2009, Imagenet: a large-scale hierarchical image database. In: *2009 IEEE Conference on Computer Vision and Pattern Recognition*, 248. DOI.

Eyles, C.J., Harrison, R.A., Davis, C.J., Waltham, N.R., Shaughnessy, B.M., Mapson-Menard, H.C.A., Bewsher, D., Crothers, S.R., Davies, J.A., Simnett, G.M., Howard, R.A., Moses, J.D., Newmark, J.S., Socker, D.G., Halain, J.-P., Defise, J.-M., Mazy, E., Rochus, P.: 2009, The Heliospheric Imagers onboard the STEREO Mission. *Sol. Phys.* **254**, 387. DOI. ADS.

Farias, H., Ortiz, D., Damke, G., Jaque Arancibia, M., Solar, M.: 2020, Mask galaxy: morphological segmentation of galaxies. *Astron. Comput.* **33**, 100420. DOI. ADS.

Feng, L., Inhester, B., Mierla, M.: 2013, Comparisons of CME morphological characteristics derived from five 3D reconstruction methods. *Sol. Phys.* **282**, 221. DOI. ADS.

Gafeira, R., Orozco Suárez, D., Milić, I., Quintero Noda, C., Ruiz Cobo, B., Uitenbroek, H.: 2021, Machine learning initialization to accelerate Stokes profile inversions. *Astron. Astrophys.* **651**, A31. DOI. ADS.

Gopalswamy, N., Yashiro, S., Michalek, G., Stenborg, G., Vourlidas, A., Freeland, S., Howard, R.: 2009, The SOHO/LASCO CME catalog. *Earth Moon Planets* **104**(1–4), 295. DOI. ADS.

Gopalswamy, N., Christe, S., Fung, S.F., Gong, Q., Gruesbeck, J.R., Jian, L.K., Kanekal, S.G., Kay, C., Kucera, T.A., Leake, J.E., Li, L., Mäkelä, P., Nikulla, P., Reginald, N.L., Shih, A., Tadikonda, S.K., Viall, N., Wilson, L.B., Yashiro, S., Golub, L., DeLuca, E., Reeves, K., Sterling, A.C., Winebarger, A.R., DeForest, C., Hassler, D.M., Seaton, D.B., Desai, M.I., Mokashi, P.S., Lazio, J., Jensen, E.A., Manchester, W.B., Sachdeva, N., Wood, B., Kooi, J., Hess, P., Wexler, D.B., Bale, S.D., Krucker, S., Hurlburt, N., DeRosa, M., Gosain, S., Jain, K., Kholikov, S., Petrie, G.J.D., Pevtsov, A., Tripathy, S.C., Zhao, J., Scherrer, P.H., Rajaguru, S.P., Woods, T., Kenney, M., Zhang, J., Scolini, C., Cho, K.-S., Park, Y.-D., Jackson, B.V.: 2024, The multiview observatory for solar terrestrial science (MOST). *J. Atmos. Sol.-Terr. Phys.* **254**, 106165. DOI. ADS.

Goussies, N., Stenborg, G., Vourlidas, A., Howard, R.: 2010, Tracking of coronal white-light events by texture. *Sol. Phys.* **262**(2), 481. DOI. ADS.

Green, L.M., Török, T., Vršnak, B., Manchester, W., Veronig, A.: 2018, The origin, early evolution and predictability of solar eruptions. *Space Sci. Rev.* **214**, 46. DOI. ADS.

He, K., Zhang, X., Ren, S., Sun, J.: 2015, Deep residual learning for image recognition. arXiv e-prints. arXiv. DOI. ADS.

He, K., Gkioxari, G., Dollár, P., Girshick, R.: 2017, Mask R-CNN. arXiv e-prints. arXiv. DOI. ADS.

Howard, R.A., Vourlidas, A.: 2018, Evolution of CME mass in the corona. *Sol. Phys.* **293**(4), 55. DOI. ADS.

Howard, R.A., Moses, J.D., Vourlidas, A., Newmark, J.S., Socker, D.G., Plunkett, S.P., Korendyke, C.M., Cook, J.W., Hurley, A., Davila, J.M., et al.: 2008, Sun Earth Connection Coronal and Heliospheric Investigation (SECCHI). *Space Sci. Rev.* **136**, 67. DOI.

Jackson, B.V., Buffington, A., Hick, P.P., Clover, J.M., Bisi, M.M., Webb, D.F.: 2010, SMEI 3D reconstruction of a coronal mass ejection interacting with a corotating solar wind density enhancement: the 2008 April 26 CME. *Astrophys. J.* **724**, 829. DOI. ADS.

Joshi, A.D., Srivastava, N.: 2011, Acceleration of coronal mass ejections from three-dimensional reconstruction of STEREO images. *Astrophys. J.* **739**, 8. DOI. ADS.

Judge, P.G., Casini, R., Tomczyk, S., Edwards, D.P., Francis, E.: 2001, Coronal magnetometry: a feasibility study. Technical report. ADS.

Kay, C., Palmerio, E.: 2024, Collection, collation, and comparison of 3d coronal cme reconstructions. *Space Weather* **22**, e2023SW003796. DOI.

Lin, T.-Y., Maire, M., Belongie, S., Bourdev, L., Girshick, R., Hays, J., Perona, P., Ramanan, D., Zitnick, C.L., Dollár, P.: 2014, Microsoft COCO: common objects in context. arXiv e-prints. arXiv. DOI. ADS.

Lin, R., Yang, Y., Shen, F., Pi, G., Li, Y.: 2024, An algorithm for the determination of coronal mass ejection kinematic parameters based on machine learning. *Astron. Astrophys. Suppl. Ser.* **271**(2), 59. DOI. ADS.

López-Cano, D., Stücker, J., Pellejero Ibañez, M., Angulo, R.E., Franco-Barranco, D.: 2024, Characterizing structure formation through instance segmentation. *Astron. Astrophys.* **685**, A37. DOI. ADS.

McKay, M.D., Beckman, R.J., Conover, W.J.: 1979, A comparison of three methods for selecting values of input variables in the analysis of output from a computer code. *Technometrics* **21**(2), 239. http://www.jstor.org/stable/1268522.

Mierla, M., Inhester, B., Marqué, C., Rodriguez, L., Gissot, S., Zhukov, A.N., Berghmans, D., Davila, J.: 2009, On 3D reconstruction of coronal mass ejections: I. Method description and application to SECCHI-COR data. *Sol. Phys.* **259**, 123. DOI. ADS.

Mierla, M., Inhester, B., Antunes, A., Boursier, Y., Byrne, J.P., Colaninno, R., Davila, J., de Koning, C.A., Gallagher, P.T., Gissot, S., Howard, R.A., Howard, T.A., Kramar, M., Lamy, P., Liewer, P.C., Maloney, S., Marqué, C., McAteer, R.T.J., Moran, T., Rodriguez, L., Srivastava, N., St. Cyr, O.C., Stenborg, G., Temmer, M., Thernisien, A., Vourlidas, A., West, M.J., Wood, B.E., Zhukov, A.N.: 2010, On the 3-D reconstruction of coronal mass ejections using coronagraph data. *Ann. Geophys.* **28**, 203. DOI. ADS.

Milić, I., Gafeira, R.: 2020, Mimicking spectropolarimetric inversions using convolutional neural networks. *Astron. Astrophys.* **644**, A129. DOI. ADS.

Morrill, J.S., Korendyke, C.M., Brueckner, G.E., Giovane, F., Howard, R.A., Koomen, M., Moses, D., Plunkett, S.P., Vourlidas, A., Esfandiari, E., Rich, N., Wang, D., Thernisien, A.F., Lamy, P., Llebaria, A., Biesecker, D., Michels, D., Gong, Q., Andrews, M.: 2006, Calibration of the Soho/Lasco C3 White Light Coronagraph. *Sol. Phys.* **233**(2), 331. DOI. ADS.

Olmedo, O., Zhang, J., Wechsler, H., Poland, A., Borne, K.: 2008, Automatic detection and tracking of coronal mass ejections in coronagraph time series. *Sol. Phys.* **248**, 485. DOI.

Otsu, N.: 1979, A threshold selection method from gray-level histograms. *IEEE Trans. Syst. Man Cybern.* **9**(1), 62. DOI.

Palomba, M., Luntama, J.-P.: 2022, Vigil: ESA Space Weather Mission in L5. In: *44th COSPAR Scientific Assembly. Held 16–24 July* **44**, 3544. ADS.

Pearce-Casey, R., Nagam, B.C., Wilde, J., Busillo, V., Ulivi, L., Andika, I.T., Manjón-García, A., Leuzzi, L., Matavulj, P., Serjeant, S., Walmsley, M., Acevedo Barroso, J.A., O'Riordan, C.M., Clément, B., Tortora, C., Collett, T.E., Courbin, F., Gavazzi, R., Metcalf, R.B., Cabanac, R., Courtois, H.M., Crook-Mansour, J., Delchambre, L., Despali, G., Ecker, L.R., Franco, A., Holloway, P., Jahnke, K., Mahler, G., Marchetti, L., Melo, A., Meneghetti, M., Müller, O., Nucita, A.A., Pearson, J., Rojas, K., Scarlata, C., Schuldt, S., Sluse, D., Suyu, S.H., Vaccari, M., Vegetti, S., Verma, A., Vernardos, G., Bolzonella, M., Kluge, M., Saifollahi, T., Schirmer, M., Stone, C., Paulino-Afonso, A., Bazzanini, L., Hogg, N.B., Koopmans, L.V.E., Kruk, S., Mannucci, F., Bromley, J.M., Dí az-Sánchez, A., Dickinson, H.J., Powell, D.M., Bouy, H., Laureijs, R., Altieri, B., Amara, A., Andreon, S., Baccigalupi, C., Baldi, M., Balestra, A., Bardelli, S., Battaglia, P., Bonino, D., Branchini, E., Brescia, M., Brinchmann, J., Caillat, A., Camera, S., Capobianco, V., Carbone, C., Carretero, J., Casas, S., Castellano, M., Castignani, G., Cavuoti, S., Cimatti, A., Colodro-Conde, C., Congedo, G., Conselice, C.J., Conversi, L., Copin, Y., Cropper, M., Da Silva, A., Degaudenzi, H., De Lucia, G., Di Giorgio, A.M., Dinis, J., Dubath, F., Dupac, X., Dusini, S., Farina, M., Farrens, S., Faustini, F., Ferriol, S., Frailis, M., Franceschi, E., Galeotta, S., George, K., Gillard, W., Gillis, B., Giocoli, C., Gómez-Alvarez, P., Grazian, A., Grupp, F., Haugan, S.V.H., Holmes, W., Hook, I., Hormuth, F., Hornstrup, A., Hudelot, P., Jhabvala, M., Joachimi, B., Keihänen, E., Kermiche, S., Kiessling, A., Kilbinger, M., Kubik, B., Kümmel, M., Kunz, M., Kurki-Suonio, H., Le Mignant, D., Ligori, S., Lilje, P.B., Lindholm, V., Lloro, I., Maiorano, E., Mansutti, O., Marggraf, O., Markovic, K., Martinelli, M., Martinet, N., Marulli, F., Massey, R., Medinaceli, E., Mei, S., Melchior, M., Mellier, Y., Merlin, E., Meylan, G., Moresco, M., Moscardini, L., Nakajima, R., Neissner, C., Nichol, R.C., Niemi, S.-M., Nightingale, J.W., Padilla, C., Paltani, S., Pasian, F., Pedersen, K., Percival, W.J., Pettorino, V., Pires, S., Polenta, G., Poncet, M., Popa, L.A., Pozzetti, L., Raison, F., Renzi, A., Rhodes, J., Riccio, G., Romelli, E., Roncarelli, M., Rossetti, E., Saglia, R., Sakr, Z., Sánchez, A.G., Sapone, D., Sartoris, B., Schneider, P., Schrabback, T., Secroun, A., Seidel, G., Serrano, S., Sirignano, C., Sirri, G., Skottfelt, J., Stanco, L., Steinwagner, J., Tallada-Crespí, P., Tereno, I., Toledo-Moreo, R., Torradeflot, F., Tutusaus, I., Valentijn, E.A., Valenziano, L., Vassallo, T., Verdoes Kleijn, G., Veropalumbo, A., Wang, Y., Weller, J., Zamorani, G., Zucca, E.: 2025, Euclid: searches for strong gravitational lenses using convolutional neural nets in early release observations of the Perseus field. *Astron. Astrophys.* **696**, A214. DOI. ADS.

Pluta, A., Mrotzek, N., Vourlidas, A., Bothmer, V., Savani, N.: 2019, Combined geometrical modelling and white-light mass determination of coronal mass ejections. *Astron. Astrophys.* **623**, A139. DOI. ADS.

Reinke, A., Tizabi, M.D., Sudre, C.H., Eisenmann, M., Rädsch, T., Baumgartner, M., Acion, L., Antonelli, M., Arbel, T., Bakas, S., Bankhead, P., Benis, A., Blaschko, M., Buettner, F., Cardoso, M.J., Chen, J., Cheplygina, V., Christodoulou, E., Cimini, B., Collins, G.S., Engelhardt, S., Farahani, K., Ferrer, L., Galdran, A., van Ginneken, B., Glocker, B., Godau, P., Haase, R., Hamprecht, F., Hashimoto, D.A., Heckmann-Nötzel, D., Hirsch, P., Hoffman, M.M., Huisman, M., Isensee, F., Jannin, P., Kahn, C.E., Kainmueller, D., Kainz, B., Karargyris, A., Karthikesalingam, A., Kavur, A.E., Kenngott, H., Kleesiek, J., Kleppe, A., Kohler, S., Kofler, F., Kopp-Schneider, A., Kooi, T., Kozubek, M., Kreshuk, A., Kurc, T., Landman, B.A., Litjens, G., Madani, A., Maier-Hein, K., Martel, A.L., Mattson, P., Meijering, E., Menze, B., Moher, D., Moons, K.G.M., Müller, H., Nichyporuk, B., Nickel, F., Alican Noyan, M., Petersen, J., Polat, G., Rafelski, S.M., Rajpoot, N., Reyes, M., Rieke, N., Riegler, M., Rivaz, H., Saez-Rodriguez, J., Sánchez, C.I., Schroeter, J., Saha, A., Selver, M.A., Sharan, L., Shetty, S., van Smeden, M., Stieltjes, B., Summers, R.M., Taha, A.A., Tiulpin, A., Tsaftaris, S.A., Van Calster, B., Varoquaux, G., Wiesenfarth, M., Yaniv, Z.R., Jäger, P., Maier-Hein, L.: 2021, Common limitations of image processing metrics: a picture story. arXiv e-prints. arXiv. DOI. ADS.

Ren, S., He, K., Girshick, R., Sun, J.: 2015, Faster R-CNN: towards real-time object detection with region proposal networks. arXiv e-prints. arXiv. DOI. ADS.

Robbrecht, E., Patsourakos, S., Vourlidas, A.: 2009, No trace left behind: STEREO observation of a coronal mass ejection without low coronal signatures. *Astrophys. J.* **701**, 283. DOI.

Rochus, P., Auchère, F., Berghmans, D., Harra, L., Schmutz, W., Schühle, U., Addison, P., Appourchaux, T., Aznar Cuadrado, R., Baker, D., Barbay, J., Bates, D., BenMoussa, A., Bergmann, M., Beurthe, C., Borgo, B., Bonte, K., Bouzit, M., Bradley, L., Büchel, V., Buchlin, E., Büchner, J., Cabé, F., Cadiergues,

L., Chaigneau, M., Chares, B., Choque Cortez, C., Coker, P., Condamin, M., Coumar, S., Curdt, W., Cutler, J., Davies, D., Davison, G., Defise, J.-M., Del Zanna, G., Delmotte, F., Delouille, V., Dolla, L., Dumesnil, C., Dürig, F., Enge, R., François, S., Fourmond, J.-J., Gillis, J.-M., Giordanengo, B., Gissot, S., Green, L.M., Guerreiro, N., Guilbaud, A., Gyo, M., Haberreiter, M., Hafiz, A., Hailey, M., Halain, J.-P., Hansotte, J., Hecquet, C., Heerlein, K., Hellin, M.-L., Hemsley, S., Hermans, A., Hervier, V., Hochedez, J.-F., Houbrechts, Y., Ihsan, K., Jacques, L., Jérôme, A., Jones, J., Kahle, M., Kennedy, T., Klaproth, M., Kolleck, M., Koller, S., Kotsialos, E., Kraaikamp, E., Langer, P., Lawrenson, A., Le Clech', J.-C., Lenaerts, C., Liebecq, S., Linder, D., Long, D.M., Mampaey, B., Markiewicz-Innes, D., Marquet, B., Marsch, E., Matthews, S., Mazy, E., Mazzoli, A., Meining, S., Meltchakov, E., Mercier, R., Meyer, S., Monecke, M., Monfort, F., Morinaud, G., Moron, F., Mountney, L., Müller, R., Nicula, B., Parenti, S., Peter, H., Pfiffner, D., Philippon, A., Phillips, I., Plesseria, J.-Y., Pylyser, E., Rabecki, F., Ravet-Krill, M.-F., Rebellato, J., Renotte, E., Rodriguez, L., Roose, S., Rosin, J., Rossi, L., Roth, P., Rouesnel, F., Roulliay, M., Rousseau, A., Ruane, K., Scanlan, J., Schlatter, P., Seaton, D.B., Silliman, K., Smit, S., Smith, P.J., Solanki, S.K., Spescha, M., Spencer, A., Stegen, K., Stockman, Y., Szwec, N., Tamiatto, C., Tandy, J., Teriaca, L., Theobald, C., Tychon, I., van Driel-Gesztelyi, L., Verbeeck, C., Vial, J.-C., Werner, S., West, M.J., Westwood, D., Wiegelmann, T., Willis, G., Winter, B., Zerr, A., Zhang, X., Zhukov, A.N.: 2020, The Solar Orbiter EUI instrument: the Extreme Ultraviolet Imager. *Astron. Astrophys.* **642**, A8. DOI. ADS.

Ronneberger, O., Fischer, P., Brox, T.: 2015, U-Net: convolutional networks for biomedical image segmentation. arXiv e-prints. arXiv. DOI. ADS.

Sarkar, R., Srivastava, N., Mierla, M., West, M.J., D'Huys, E.: 2019, Evolution of the coronal cavity from the quiescent to eruptive phase associated with coronal mass ejection. *Astrophys. J.* **875**(2), 101. DOI. ADS.

Shan, J., Zhang, H., Lu, L., Zhang, Y., Feng, L., Ge, Y., Xue, J., Li, S.: 2024, Camel. II. A 3D coronal mass ejection catalog based on coronal mass ejection automatic detection with deep learning. *Astrophys. J. Suppl. Ser.* **272**(1), 18. DOI.

Sheeley, J.N.R., Howard, R.A., Koomen, M.J., Michels, D.J., Harvey, K.L., Harvey, J.W.: 1982, Observations of coronal structure during sunspot maximum. *Space Sci. Rev.* **33**(1–2), 219. DOI. ADS.

Sieyra, M.V., Cécere, M., Cremades, H., Iglesias, F.A., Sahade, A., Mierla, M., Stenborg, G., Costa, A., West, M.J., D'Huys, E.: 2020, Analysis of large deflections of prominence-cme events during the rising phase of solar cycle 24. *Sol. Phys.* **295**(9), 126. DOI. ADS.

Simonyan, K., Zisserman, A.: 2014, Very deep convolutional networks for large-scale image recognition. arXiv e-prints. arXiv. DOI. ADS.

Sokolov, I.V., van der Holst, B., Oran, R., Downs, C., Roussev, I.I., Jin, M., Manchester, W.B. IV, Evans, R.M., Gombosi, T.I.: 2013, Magnetohydrodynamic waves and coronal heating: unifying empirical and MHD turbulence models. *Astrophys. J.* **764**(1), 23. DOI. ADS.

Thernisien, A.F.R., Howard, R.A., Vourlidas, A.: 2006, Modeling of flux rope coronal mass ejections. *Astrophys. J.* **652**, 763. DOI. ADS.

Thernisien, A., Vourlidas, A., Howard, R.A.: 2009, Forward modeling of coronal mass ejections using STEREO/SECCHI data. *Sol. Phys.* **256**, 111. DOI. ADS.

Thernisien, A., Vourlidas, A., Howard, R.A.: 2011, CME reconstruction: pre-STEREO and STEREO era. *J. Atmos. Sol.-Terr. Phys.* **73**, 1156. DOI. ADS.

Thernisien, A.F., Chua, D.H., Carter, M.T., Rich, N.B., Noya, M., Babich, T.A., Crippa, C.E., Baugh, B., Bordlemay, Y., Socker, D., Biesecker, D., Korendyke, C., Wang, D., Vassiliadis, D., Wang, N.-Y., Abbay, S., Bagnall, S., Balmaceda, L., Brown, S., Bonafede, J., Boyer, D., Declet, J., Cheng, P., Corsi, K., Cremerius, L., Chavis, I., Chiralo, J., Clifford, G., Dancheck, J., Davis, J., Dima, G., Dudley, R., Gardner, D., Gardner, L., Hagood, B., Hagood, R., Hohl, B., Hunt, T., Jenkins, F., Johnson, J.M., Koehler, M., Kuroda, N., Lanagan, A., Laut, S., Lynch, B., Mallory, T., Mechel, D., Miles, N.D., Miranda, A., Newman, M., Nguyen, B., Ogindo, M., Pellak, K., Podgurski, R., Ragan, T., Richards, V., Silver, D., Simmons, J., Schmit, D.J., Smith, L., Spitzak, J., Tadikonda, S.K., Tanner, S., Uhl, D., Verzosa, J., Walker, P., Wiggins, G., Williams, E., Wilson, C., Zurcher, D.: 2025, The CCOR compact coronagraphs for the Geostationary Operational Environmental Satellite-19 (GOES-19) and the Space Weather Follow on (SWFO) Missions. arXiv e-prints. arXiv. DOI. ADS.

Titov, V.S., Török, T., Mikic, Z., Linker, J.A.: 2014, A method for embedding circular force-free flux ropes in potential magnetic fields. *Astrophys. J.* **790**(2), 163. DOI. ADS.

Tripathi, D., Raouafi, N.-E.: 2007, On the relationship between coronal waves associated with a CME on 5 March 2000. *Astron. Astrophys.* **473**(3), 951. DOI. ADS.

van der Holst, B., Sokolov, I.V., Meng, X., Jin, M., Manchester, W.B. IV, Tóth, G., Gombosi, T.I.: 2014, Alfvén Wave Solar Model (AWSoM): coronal heating. *Astrophys. J.* **782**, 81. DOI. ADS.

Verbeke, C., Mays, M.L., Kay, C., Riley, P., Palmerio, E., Dumbović, M., Mierla, M., Scolini, C., Temmer, M., Paouris, E., Balmaceda, L.A., Cremades, H., Hinterreiter, J.: 2022, Quantifying errors in 3d cme

parameters derived from synthetic data using white-light reconstruction techniques. *Adv. Space Res.*. DOI. https://www.sciencedirect.com/science/article/pii/S027311772200792X.
Vourlidas, A., Webb, D.F.: 2018, Streamer-blowout coronal mass ejections: their properties and relation to the coronal magnetic field structure. *Astrophys. J.* **861**(2), 103. DOI. ADS.
Vourlidas, A., Subramanian, P., Dere, K.P., Howard, R.A.: 2000, Large-angle spectrometric coronagraph measurements of the energetics of coronal mass ejections. *Astrophys. J.* **534**, 456. DOI. ADS.
Vourlidas, A., Wu, S.T., Wang, A.H., Subramanian, P., Howard, R.A.: 2003, Direct detection of a coronal mass ejection-associated shock in large angle and spectrometric coronagraph experiment white-light images. *Astrophys. J.* **598**(2), 1392. DOI. ADS.
Vourlidas, A., Sanchez Andrade-Nuño, B., Landi, E., Patsourakos, S., Teriaca, L., Schühle, U., Korendyke, C.M., Nestoras, I.: 2010, The structure and dynamics of the upper chromosphere and lower transition region as revealed by the subarcsecond VAULT observations. *Sol. Phys.* **261**, 53. DOI. ADS.
Vourlidas, A., Lynch, B.J., Howard, R.A., Li, Y.: 2013, How many CMEs have flux ropes? Deciphering the signatures of shocks, flux ropes, and prominences in coronagraph observations of CMEs. *Sol. Phys.* **284**, 179. DOI.
Vourlidas, A., Balmaceda, L.A., Stenborg, G., Dal Lago, A.: 2017, Multi-viewpoint coronal mass ejection catalog based on STEREO COR2 observations. *Astrophys. J.* **838**(2), 141. DOI. ADS.
Vršnak, B., Warmuth, A., Temmer, M., Veronig, A., Magdalenić, J., Hillaris, A., Karlický, M.: 2006, Multi-wavelength study of coronal waves associated with the CME-flare event of 3 November 2003. *Astron. Astrophys.* **448**(2), 739. DOI. ADS.
Wang, P., Zhang, Y., Feng, L., Yuan, H., Gan, Y., Li, S., Lu, L., Ying, B., Gan, W., Li, H.: 2019, A new automatic tool for cme detection and tracking with machine-learning techniques. *Astrophys. J. Suppl. Ser.* **244**(1), 9. DOI.
Wang, X.-L., Fang, M., Gao, Y., Zhang, H.-X., Herczeg, G.J., Ma, H.-J., Chen, E., Zhou, X.-Y.: 2022, Distributed YSOs in the Perseus Molecular Cloud from the Gaia and LAMOST surveys. *Astrophys. J.* **936**(1), 23. DOI. ADS.
Webb, D.F., Howard, T.A.: 2012, Coronal mass ejections: observations. *Living Rev. Sol. Phys.* **9**, 3. DOI. http://www.livingreviews.org/lrsp-2012-3.
Wei, X.-S., Zhang, C.-L., Wu, J., Shen, C., Zhou, Z.-H.: 2019, Unsupervised object discovery and co-localization by deep descriptor transformation. *Pattern Recognit.* **88**, 113. DOI. ADS.
Xia, X., Kulis, B.: 2017, W-Net: a deep model for fully unsupervised image segmentation. arXiv e-prints. arXiv. DOI. ADS.
Xie, E., Wang, W., Yu, Z., Anandkumar, A., Alvarez, J.M., Luo, P.: 2021, SegFormer: simple and efficient design for semantic segmentation with transformers. arXiv e-prints. arXiv. DOI. ADS.
Yashiro, S., Michalek, G., Gopalswamy, N.: 2008, A comparison of coronal mass ejections identified by manual and automatic methods. *Ann. Geophys.* **26**(10), 3103. DOI. ADS.
Yashiro, S., Gopalswamy, N., Michalek, G., St. Cyr, O.C., Plunkett, S.P., Rich, N.B., Howard, R.A.: 2004, A catalog of white light coronal mass ejections observed by the SOHO spacecraft. *J. Geophys. Res. Space Phys.* **109**, 7105. DOI.
Yurchyshyn, V., Yashiro, S., Abramenko, V., Wang, H., Gopalswamy, N.: 2005, Statistical distributions of speeds of coronal mass ejections. *Astrophys. J.* **619**(1), 599. DOI. ADS.
Zhang, J., Blanco-Cano, X., Nitta, N., Srivastava, N., Mandrini, C.H.: 2018, Editorial: Earth-affecting solar transients. *Sol. Phys.* **293**, 80. DOI. ADS.

Publisher's Note Springer Nature remains neutral with regard to jurisdictional claims in published maps and institutional affiliations.

Authors and Affiliations

Francisco A. Iglesias[1,2] · Diego G. Lloveras[1,2,3,4] · Florencia L. Cisterna[1] · Hebe Cremades[1,2] · Mariano Sanchez Toledo[1] · Fernando M. López[1,2] · Yasmin Machuca[1,2] · Franco Manini[1,2] · Andrés Asensio Ramos[5]

✉ F.A. Iglesias
francisco.iglesias@um.edu.ar

✉ D.G. Lloveras
diego.lloveras@nasa.gov

[1] Grupo de Estudios en Heliofísica de Mendoza, Universidad de Mendoza, Boulogne Sur Mer 683, 5500 Mendoza, Argentina

[2] Consejo Nacional de Investigaciones Científicas y Técnicas, Godoy Cruz 2290, C1425FQB CABA, Argentina

[3] Present address: Heliophysics Science Division, NASA Goddard Space Flight Center, Greenbelt, MD 20771, USA

[4] Present address: Physics and Astronomy Department, George Mason University, 4400 University Drive, Fairfax, VA 22030, USA

[5] Instituto de Astrofísica de Canarias, 38205 La Laguna, Tenerife, Spain